Laser ablation aerosol particle time-of-flight mass spectrometer (LAAPTOF): Performance, reference spectra and classification of atmospheric samples

Xiaoli Shen[1,2], Ramakrishna Ramisetty[1], Claudia Mohr[1,3], Wei Huang[1,2], Thomas Leisner[1], Harald Saathoff[1,*]

[1]Institute of Meteorology and Climate Research (IMK-AAF), Karlsruhe Institute of Technology (KIT), Hermann-von-Helmholtz-Platz 1, 76344 Eggenstein-Leopoldshafen, Germany
[2]Institute of Geography and Geoecology (IfGG), Karlsruhe Institute of Technology (KIT), Kaiserstr.12, 76131 Karlsruhe, Germany
[3]Now at: Department of Environmental Science and Analytical Chemistry, Stockholm University, Stockholm, 11418, Sweden

Correspondence to: Harald Saathoff (harald.saathoff@kit.edu)

Abstract. The laser ablation aerosol particles time-of-flight mass spectrometer (LAAPTOF, Aeromegt GmbH) is able to identify the chemical composition and mixing state of individual aerosol particles, and thus is a tool for elucidating their impacts on human health, visibility, ecosystem and climate. The overall detection efficiency (ODE) of the instrument we use was determined to range from ~(0.01 ± 0.01)% to ~(4.23 ± 2.36)% for polystyrene latex (PSL) in the size rage of 200 to 2000 nm, ~(0.44 ± 0.19)% to ~(6.57 ± 2.38)% for ammonium nitrate (NH_4NO_3), and ~(0.14 ± 0.02)% to ~(1.46 ± 0.08)% for sodium chloride (NaCl) particles in the size rage of 300 to 1000 nm. Reference mass spectra of 32 different particle types relevant for atmospheric aerosol (e.g. pure compounds NH_4NO_3, K_2SO_4, NaCl, oxalic acid, pinic acid, and pinonic acid; internal mixtures of e.g. salts, secondary organic aerosol, and metallic core-organic shell particles; more complex particles such as soot and dust particles) were determined. Our results show that internally mixed aerosol particles can result in spectra with new clusters of ions, rather than simply a combination of the spectra from the single components. An exemplary one-day ambient data set was analysed by both classical Fuzzy clustering and a reference spectra based classification method. Resulting identified particle types were generally well correlated. We show how a combination of both methods can greatly improve the interpretation of single particle data in field measurements.

1 Introduction

Atmospheric aerosol particles impact visibility, interact with trace gases, can act as cloud condensation and ice nuclei, and influence the Earth's radiation budget (Seinfeld and Pandis, 2006). Especially the continuously evolving chemical composition of aerosol particles is of scientific interest, as it influences all aerosol effects (Burkholder et al., 2017; Pöschl, 2005). However, large knowledge gaps still exist related to the chemical composition of the organic and inorganic components and their mutual interaction (Jimenez et al., 2009; Murphy et al., 2006; Schill and Tolbert, 2013; Zhang et al., 2007).

Aerosol particles can contain various components ranging from volatile to refractory species (Pratt and Prather, 2012). The global aerosol mass burden was estimated to consist of 73.6% dust, 16.7% sea salt, 2.8% biogenic secondary organic aerosols (SOA), 2.3% primary organic aerosols (POA), 1.3% sulphate, 1.3% ammonium, 1.2% nitrate, 0.4% black carbon (soot), 0.2% anthropogenic SOA, and 0.2% methane sulphonic acid (Tsigaridis et al., 2006). During the ambient aerosols' lifetime, ranging from hours to a few weeks (Pöschl, 2005), the complexity of their chemical composition usually increases by coagulation, cloud processing, and chemical reactions (Seinfeld and Pandis, 2006; Usher et al., 2003). This modifies the particles' mixing state, with

both internal (individual particles consisting of mixed compounds, e.g. coating structures) and external mixtures (e.g. mixture of particles consisting of different compounds) (Li et al., 2016). The aforementioned findings underscore the importance of measuring aerosol chemical composition and its changes on short timescales and on a single particle basis, which can be realized by on-line mass spectrometry.

One-line mass spectrometry includes bulk and single-particle measurements (Pratt and Prather, 2012). Single particle mass spectrometry, which can be dated back to the 1970s, aims at in situ and real time identification of the chemical composition of individual aerosol particles, hereby elucidating a particle's external and internal mixing properties (Noble and Prather, 2000). Online single particle mass spectrometers (SPMS) commonly use pulsed lasers for particle desorption and ionization (LDI), with the advantage of ionizing nearly all atmospheric particle components, including both non-refractory and refractory materials (Kulkarni et al., 2011). To the best of our knowledge, so far there is no quantitative analysis of particle composition by SPMS, since the ablation/ionization laser cannot interact with the entire particle and the generated ion fragments/clusters are susceptible to matrix effects (Ramisetty et al., 2017). In addition, ionization mechanisms are not fully understood (Murphy, 2007). SPMS have identified many different ambient particle types in different regions of the atmosphere, such as an elemental carbon/organic carbon (ECOC), organic-sulphate, aged sea salt, biological, soil dust, and different metal dominated types (Dall'Osto et al., 2016; Moffet et al., 2008; Murphy et al., 2006; Schmidt et al., 2017). These measurements all confirmed the complexity of individual particles' mixing state, and demonstrated the usefulness of single particle mass spectra for apportionment of individual particle sources, including e.g. fossil fuel and biomass burning combustion, cooking, marine, and shipping sources (Arndt et al., 2016; Schmidt et al., 2017).

Currently, there are only two commercially available SPMSs, i.e. the Single Particle Aerosol Mass Spectrometer (SPAMS, Hexin Analytical Instrument Co., Ltd., China) (Li et al., 2011; Lin et al., 2017) and the Laser Ablation Aerosol Particles Time-of-Flight mass spectrometer (LAAPTOF, Aeromegt GmbH, Germany). LAAPTOF uses two laser diodes (wave length 405 nm, ~40 mW, ~50 μm beam spot diameter, Marsden et al., 2016; Zawadowicz et al., 2017) for optical counting and size recording by light scattering, and one excimer laser (ArF , 193 nm, ~ 4 mJ) for one step ablation/ionization. The overall detection efficiency (ODE) of this instrument, defined as the number of single particle mass spectra obtained from the total number of aerosol particles in the sampled air, was determined to range from ~0.15% to ~2.2% for polystyrene latex (PSL) particles with geometric diameters (d_p) between 350 nm and 800 nm (Gemayel et al., 2016; Marsden et al., 2016). The instrument used by Gemayel et al. (2016) exhibited a maximum ODE of ~2.2% for PSL particle diameters of 450 nm, while ~1% at 600 nm was the peak ODE reported by Marsden et al. (2016) before the instrument modification. The response of the LAAPTOF to spherical PSL particles smaller than 350 nm and bigger than 800 nm, and the response to other particle types with different shapes, have not been investigated systematically. The scattering efficiency (SE), defined as the number fraction of particles detected by light scattering compared to the number of particles in the sampled air in front of the aerodynamic inlet lens (ADL) of the instrument (refer to Fig. 1), is determined by the laser diodes, the detection optics, as well as the photomultiplier tubes (PMT), and has a strong influence on the ODE of the instrument. Therefore, several groups tried to improve this part of the instrument. Marsden et al. (2016) modified the detection stage geometry by replacing the detection laser with a fiber coupled 532 nm, 1 W Nd:YAG solid state laser system with a collimated laser beam, accomplishing an order of magnitude improvement in light detection sensitivity to PSL particles with 500–800 nm diameter. Zawadowicz et al. (2017) modified the optical path of the laser diodes with a better laser beam of <1 mrad full angle divergence and 100 μm detection beam spot size, and applied light guides to enhance the scattered light collection. This resulted in 2−3 orders of magnitude improvement in optical counting efficiency of incident PSL particles with 500−2000 nm vacuum aerodynamic diameter (d_{va}). There are only very few studies so far that discuss mass spectral patterns of different particle types measured by LAAPTOF. Gemayel et al. (2016) presented spectra from ambient

particles collected in the city centre of Marseille, France; spectra (positive only) from pure soot and SOA coated soot particles were shown by Ahern et al. (2016); spectra from potassium rich feldspar, soot, Argentinian soil dust, and Snomax (commercial ice nuclei) were shown by Zawadowicz et al. (2017); PSL and potassium rich feldspar spectra were measured by Marsden et al. (2018); and radiolytically formed particles spectra were measured by Wonaschuetz et al. (2017). Reitz et al. (2016) presented peak assignments for pure ammonium nitrate and sulphate particles, as well as for ambient particles measured at a suburban site of Düsseldorf, Germany, but did not show any spectra. Marker ions generated from SPMS are likely instrument specific, as pointed out by Schmidt et al. (2017). Therefore, there is a need for publicly available spectral information of this relatively new instrument.

There exists several techniques to group the large number of individual particle types and spectra resulting from SMPS measurements, such as k-means, c-means, and hierarchical clustering algorithms, neural network based methods such as ART2-A, as well as the most recent algorithm of ordering points to identify the clustering structure (OPTICS), to help analyse the data (Hinz et al., 1999; Murphy et al., 2003; Reitz et al., 2016; Zelenyuk et al., 2006b; Zhao et al., 2008). There also exist target (reference spectra/predefined clusters)-oriented methods (Hinz et al., 1999; Gleanta GmbH; LAAPTOF AnalysisPro, Aeromegt GmbH).

In this paper we have characterized our LAAPTOF instrument with respect to its ODE for PSL, NH_4NO_3, and sodium chloride (NaCl) particles for a wide size range (d_m: 200−2000 nm PSL; 300−1000 nm NH_4NO_3 and NaCl). We present laboratory based reference spectra for aerosol particles containing atmospherically relevant components, which were grouped in three categories: 1) particles consisting of pure compounds, e.g. NH_4NO_3, K_2SO_4, and organic acids; 2) particles consisting of well-defined mixtures of pure salts and mixtures of organic compounds, e.g. α-pinene SOA, and PSL internally mixed with K_2SO_4, as well as other core-shell type of particles; and 3) particles consisting of complex mixtures, e.g. soot and dust particles. These reference spectra may also provide other users comprehensive references for comparison purposes, and thus help better interpret ambient data. An example for field data analysis based on reference spectra as well as Fuzzy c-means clustering will be given in chapter 3.3.

2 Methods

2.1 The LAAPTOF instrument

The LAAPTOF has been described in several recent publications (Ahern et al., 2016; Gemayel et al., 2016; Marsden et al., 2016, 2018; Reitz et al., 2016; Wonaschuetz et al., 2017; Zawadowicz et al., 2017). Therefore, we only briefly review the general operation steps that yield size and composition information of individual aerosol particles. The LAAPTOF instrument used in this study was delivered in April 2015 and may differ in a few technical aspects from earlier or later versions. A schematic of the main LAAPTOF components is given in Fig. 1 Particles with a vacuum aerodynamic diameter (d_{va}) between ~70 nm and 2.5 μm are sampled with a sampling flowrate of ~80 standard cubic centimetre per minute (SCCM), focused and accelerated by an aerodynamic lens, ADL (LPL-2.5, Aeromegt GmbH) with close to 100% transmission efficiency for particles with d_{va} 100 nm to 2 μm (http://www.aeromegt.com/#products?LPL-2.5_details), then pass through the particle time-of-flight (PTOF) chamber in which the individual particle can be detected by two sizing laser beams (405 nm continuous wave, 40 mW) separated by 11.3 cm. Based on the particle time of flight between the two laser beams, its d_{va} can be determined and recorded. After detection by the second sizing laser, a nanosecond (ns) excimer laser pulse (wave length: 193 nm, pulse duration: 4 to 8 ns, maximum pulse energy: ~8 mJ, beam diameter: ~ 300 μm when it hits the particle (Ramisetty et al., 2017), power density: ~10^9 W·cm^{-2}, ATLEX-S, ATL Lasertechnik GmbH) can be triggered to desorb and ionize particle compounds. A laser pulse energy of 4 mJ was used

for all the measurements in this study. More details about the ionization region geometry are given by Ramisetty et al. (2017). The resulting ions are analysed by a bipolar time-of-flight mass spectrometer (BTOF-MS; TOFWERK AG; mass resolution of m/ Δ m ~600 to 800 at 184 Th, mass range m/q=1 up to ~2000 Th). The resulting cations and anions are detected by corresponding microchannel plate arrays (MCPs), producing a pair of positive and negative spectra for each single particle.

2.2 Aerosol particle generation and experimental setup in the laboratory

The laboratory based aerosol particles measured in this study (summarized in Table 1) were generated in four different ways (A, B1, B2, and S).

Method A: Samples for pure particles and homogeneous and heterogeneous mixtures were dissolved/suspended in purified water and nebulized (ATM 221; Topas GmbH) with dry synthetic air, passed through two diffusion dryers (cylinder filled with Silica gel, Topas GmbH), and then size selected by a Differential Mobility Analyser (DMA 3080, TSI GmbH) before being sampled by LAAPTOF.

Method B1: Particles were sampled from the 84.5 m^3 simulation chamber AIDA (Aerosol Interactions and Dynamics in the Atmosphere) of KIT (Saathoff et al., 2003). SOA particles were formed in the 3.7 m^3 stainless steel Aerosol Preparation and Characterization (APC) chamber via ozonolysis (~6 ppm ozone) of α-pinene (~2.2 ppm) and then transferred into AIDA. Soil dust samples were dispersed by a rotating brush generator (RBG1000, PALAS) and injected via cyclones into the AIDA chamber. Sea salt particles were generated and injected into AIDA by ultrasonically nebulizingartificial seawater (Sigma Aldrich) and highly concentrated skeletonema marinoi culture (in artificial seawater), respectively, via a droplet separator and 2 diffusion dryers (Wagner et al., 2017).

Method B2: Used only for soot particles, which were generated with a propane burner (RSG miniCAST; Jing Ltd.) and injected into and sampled from a stainless steel cylinder of 0.2 m^3 volume.

Method S: Silica, Hematite, Illite_NX, Arizona test dust, desert and urban dust, black carbon from chestnut wood (University of Zürich, Switzerland), and diesel soot reference particles from NIST were suspended in their reservoir bottles by shaking them and sampled directly from the headspace (upper part) of these reservoirs through a tube connecting it with the LAAPTOF.

For all the measurements, except measuring the method S-generated particles, a condensation particle counter (CPC 3010, TSI GmbH) was used to record the particle number concentration in parallel with the LAAPTOF inlet. Setup in Fig. 1 was specific for particles generated from method A.

2.3 Field measurement

Unusually high particle number concentrations, similar to downtown Karlsruhe (a city in southwest Germany), were observed frequently northeast of Karlsruhe by particle counters on-board a tram wagon (www.aero-tram.kit.edu) intersecting the city (Hagemann et al., 2014). To study the nature and to identify possible sources of these particles, their number, size, chemical composition, associated trace gases, and meteorological conditions were measured from July 15th to September 1st, 2016 at a rural location (49°6'10.54"N, 8°24'26.07"E), next to the tram line north of the village of Leopoldshafen, Germany. Ambient aerosol particles were sampled through a $PM_{2.5}$ inlet (SH 2.5 - 16, Comde-Derenda GmbH) with 1 m^3 h^{-1}, a fraction of which was guided into the LAAPTOF, which was deployed for ~5 weeks from July 26 to August 31. LAAPTOF measurements provided information on size and mass spectral patterns for individual particles. In this paper we use data from one day as an example for the potential interpretation of LAAPTOF spectral data using reference spectra.

2.4 Efficiency calculations

In the literature there are two definitions of detection efficiency (DE) of SPMS used: one is equal to the scattering efficiency (SE) of the detection lasers (Brands et al., 2011; Gaie-Levrel et al., 2012; Su et al., 2004; Zelenyuk and Imre, 2005; Zelenyuk et al., 2009), which is the fraction of particles detected by the scattering optics in the detection region of the instrument; the other one is the product of SE and hit rate (HR) of the ablation/ionization laser (Su et al., 2004; Gemayel et al., 2016; Marsden et al., 2016). The hit rate is the fraction of particles detected leading actually to a useful mass spectrum. In this paper we use overall detection efficiency (ODE), defined by the following equations:

$$ODE = SE \times HR \times 100\% \quad (1)$$

$$SE = N_d/N_0 \times 100\% \text{ (transmission efficiency of ADL is included)} \quad (2)$$

$$HR = N_s/N_d \times 100\% \text{ (ionization efficiency is included)} \quad (3)$$

$$N_0 = C_n \times \text{flowrate} \times \text{time} \quad (4)$$

where N_d is the number of particles detected by light scattering, N_0 is the number of particles in front of the ADL, N_s the number of bipolar spectra, C_n is the particle number concentration (cm^{-3}) measured by a CPC in front of the ADL and the flowrate is the LAAPTOF sample flowrate.

2.5 Spectral and size data analysis

For each type of laboratory generated aerosol particles, we measured at least 300 mass spectra. Data analysis is done via the LAAPTOF Data Analysis Igor software (Version 1.0.2, Aeromegt GmbH). There are five main steps for the basic analysis procedure: a) removal of the excimer laser ringing signal from the raw mass spectra; b) determination of the signal baseline; c) filtering for empty spectra; d) mass calibration; and e) stick integration, that is the integration of nominal masses for peaks. It should be noted that spectrum-to-spectrum differences in peak positions for the same ion fragments/clusters complicate the mass calibrations. This may be caused by differences in kinetic energy of the ions produced, however this effect is typically compensated in the TOFs with reflectron (Kulkarni et al., 2011). Spectrum-to-spectrum peak shifts, especially in the positive spectra in our study, are mainly because of variance in the position of particle-laser interaction, which cannot be corrected with the existing Aeromegt software or the LAAPTOF instrument (Ramisetty et al., 2017). Details can be found in 'Procedure 1' in the supplementary information. Spectra presented in this paper were typically normalized to the sum of ion signal before further aggregation.

For ambient data analysis, we used two different classification methods. The first one is Fuzzy c–means clustering algorithm embedded in the LAAPTOF Data Analysis Igor software, commonly used to do classification based on the similarities of the individual spectra. The number of the classes is chosen manually, afterwards the particle spectra with a minimum distance between their data vectors and a cluster centre will be grouped into a specific class (Hinz et al., 1999; Reitz et al., 2016). Since each spectrum can belong to multiple classes (Reitz et al., 2016) the resulting fraction/percentage for each class represents the information about the degree of similarity between aerosol particles in one particular class, and not a number percentage. The second method developed in this study is based on the correlation between each ambient spectrum and our reference spectra. The resulting Pearson's correlation coefficient (r) is used as the criterion to group particles into different types (here we use "types" instead of "classes" in order to differentiate these two classification methods). When r is higher than a threshold value of 0.6, the ambient spectrum is considered to have high correlation with the corresponding reference spectrum. For simplification we chose 10 positive and 7 negative reference spectra. For example, we only use German soil dust as the reference for arable soil dust rather than using four arable soil dust samples from different places. More details about the procedure for this method as well as the corresponding equations and uncertainties estimation can be found in "Procedure 2" in the supplementary information.

In addition, particle size (d_{va}) was recorded for individual particles. The corresponding size distribution can be plotted as d_{va} histogram, a Gaussian fit of which yields number mean d_{va} values and the standard deviation (width).

3 Results and Discussion

3.1 LAAPTOF performance

3.1.1 Hit rate, scattering efficiency and overall detection efficiency for standard samples

Hit rate (HR), scattering efficiency (SE), and overall detection efficiency (ODE) for spherical PSL particles as a function of electrical mobility equivalent diameter d_m, are plotted in Fig. 2. It should be noted that the LAAPTOF detection behaviour may vary depending on the alignment of the ADL and the optical components (especially the detection laser diodes), which is difficult to reproduce. We therefore show results for PSL particles based on 2 repeated experiments after 3 alignments each, and thus a total of 6 experiments for each data point. The uncertainty intervals in Fig. 2 are the difference between the maximum/minimum and the average values obtained from these 6 experiments. As shown in panel A of Fig. 2, for particle diameters from 200 to 400 nm, HR_{PSL} exhibits an increase from 69% to 94%, decreases to 83% for 700 nm particles, and then becomes stable at ~85% for particles with diameters up to 2 µm. The average HR_{PSL} ($\overline{HR}_{PSL}$) is ~84%. SE_{PSL} and ODE_{PSL} show an M-like shape with two peaks, at 500 nm (SE_{PSL} 3.0%, ODE_{PSL} 2.7%), and at 1000 nm (SE_{PSL} 4.8%, ODE_{PSL} 4.2) (see panel B and C of Fig. 2). We attribute this behaviour to a combined effect of the spherical shape of PSL particles and the optical system of this instrument, e.g. Mie resonances related to particle size and laser wavelength (see section 3.1.2 for details). As shown in panel C of Fig. 2, values and trends of ODE_{PSL} in the size range of 300−800 nm of our instrument are similar to those reported by Gemayel et al. (2016) and Marsden et al. (2016) for their LAAPTOF instruments. A recent LAAPTOF study by Zawadowicz et al. (2017) shows comparable results for PSL particles with $d_p \leq 500$ nm, and an M-like shape of ODE in the size range of 200−2000 nm (after instrument modification).

We also measured mass spectra of non-spherical NH_4NO_3 (χ=0.8, Williams et al., 2013) and NaCl particles (cubic, χ=1.06 to 1.17, Zelenyuk et al., 2006a). Similar as for PSL particles, NH_4NO_3, and NaCl particles show relatively high and stable HR with average values of 80% and 66% (see panel D in Fig. 2), thus SE and ODE have a similar trend. No M-like shape of ODE as a function of particle size is observed due to the different light scattering properties of the non-spherical salt particles (Bohren and Huffman, 2007) (see panels E and F in Fig. 2). Comparable results were shown for $(NH_4)_2SO_4$ particles (χ=1.03 to 1.07, Zelenyuk et al., 2006a) by Zawadowicz et al. (2017). As shown in Fig. 2 E–F, SE and ODE decrease with increasing shape factor for salt particles of the same size. We will discuss this in more detail in the following section.

3.1.2 Factors influencing overall detection efficiency

There are various factors that can influence the ODE of LAAPTOF. One of these is particle size. For particles with diameters below 200 nm, the scattered light becomes too weak to be detected due to the strong dependence of the scattering intensity on particle size (Bohren and Huffman, 2007). For particles with diameters larger than 2 µm, focusing by the ADL is much less efficient, resulting in a higher divergence of the particle beam (Schreiner et al., 1999). This lowers the probability of larger particles to be detected by the detection/scattering laser and/or to be hit by the ionization laser. In addition, light scattering of spherical particles like PSL changes from Rayleigh to Mie to Geometric scattering as the size parameter $\alpha=\pi d_p/\lambda$ increases from $<<1$ to ~1 to $>>1$ (Seinfeld and Pandis, 2006). The scattering efficiencies of PSL particles, based on Mie calculation at the particle sizes and detection laser wavelength relevant to our LAAPTOF measurement, validate the M-like shape of SE_{PSL} (refer to Fig. S1). As long as the particle diameter (d_p) is smaller than the wavelength of the detection laser light, here 405 nm, the

scattered radiation intensity (proportional to d_p^6) will rapidly decrease with decreasing particle sizes, resulting in low ODE. ODE is e.g. 0.01% for 200 nm PSL particles. For non-spherical particles like salts, their SE and ODE are also size dependent (panel F in Fig. 2), due to size-dependent light scattering ability and particle beam divergence. However, in the size range of 300 to 1000 nm studied here, they don't exhibit Mie resonance and thus don't show an M-like shape in their scattering efficiency.

Optical properties of the particles have a strong impact on how light is scattered and absorbed, and thus it should be noted that the optical properties do not only influence scattering efficiency, but also absorption and ionization efficiency (or hit rate). As shown in Fig. 2F, ODE for NH_4NO_3 is higher than that for NaCl at any size we studied. This is mainly caused by differences in their optical properties of scattering. Fresh soot particles scatter only little light due to their black colour and small size (typically ~ 20 nm) of the primary particles forming their agglomerates, and are thus hardly detected by the detection laser. However they are good light absorbers and thus relatively easy to ablate and ionize. The reference spectra of pure NH_4NO_3 and $(NH_4)_2SO_4$ particles showed intensive prominent peaks for pure NH_4NO_3 particles (refer to Fig. 3A) but only one weak peak of m/z 30 NO^+ for pure $(NH_4)_2SO_4$ particles. This indicates that NH_4NO_3 is a better absorber than $(NH_4)_2SO_4$, and thus easier to ablate and ionize. For homogeneous mixtures of these two ammonium salts, the sulphate species are ablated and ionized much more easily (refer to section 3.2.2), due to increased UV light absorption by the nitrate component. Some small organic compounds with weak absorption properties are hard to ablate and ionize, e.g. oxalic acid ($C_2H_2O_4$), pinic acid, and cis-pinonic acid. They exhibited much weaker signals (~80% lower) than macromolecular organic compounds in PSL or humic acid particles.

Particle morphology is another important factor. The scattering efficiency for non-spherical NH_4NO_3 is higher than for spherical PSL particles in the size rage of 300–800 nm (Fig. 2 B–E) (Ackerman et al., 2015). For larger particle sizes (d_m> 800 nm), beam divergence offsets the shape effect (Murphy, 2007). Apart from that, the increase of surface roughness and inhomogeneity can promote the scattering capability of particles (Ackerman et al., 2015).

The incident intensity of radiation, which is another parameter that influences the light scattered by particles (as well as background signal caused by stray light), is related to power and beam dimensions of the detection laser. Corresponding instrument modifications were done by Marsden et al. (2016) and Zawadowicz et al. (2017) (refer to section 1). In addition, alignment of the excimer laser focus in x, y, and z position influences optimum hit rates (Ramisetty et al., 2017).

There are further instrumental aspects that affect the detection efficiency. High number concentrations of the incoming particles influence the ODE, since there can be more than one particle present between the two detection lasers. The transmission efficiency of the ADL is included in the scattering efficiency, and thus directly influences it. The size range of particles focused in the lens, and the particle beam width strongly depend on the configuration of the ADL (Canagaratna et al., 2007; Johnston, 2000). Liu lenses and Schreiner lenses can focus the particles in the size range of 80−800 nm, and 300−3000 nm, respectively (Kamphus et al., 2008; Liu et al., 1995; Schreiner et al., 1999). The ADL transmission efficiency of our instrument, as determined by the manufacturer (Aeromegt GmbH), is close to 100% for particles with d_{va} 100–2000 nm.

3.2 LAAPTOF reference spectra of laboratory generated particle types

Particles for which reference spectra are presented here are listed in Table 1. For each type of these aerosol particles, we present averaged spectra for typically 300 to 500 single particles. The relative standard deviations (RSD, SD normalized to signal) for the characteristic peaks are in the range of 15−186%, median value 77%.

Despite the lack of full quantitativeness of the LAAPTOF, mass spectral signal amplitudes show an increase with particle size (refer to Fig. S2). However, no systematic changes in the mass spectral signatures were observed for different particle sizes. Therefore, for the samples passing through the DMA, particles in the optimum size range of the LAAPTOF (d_m = 800 nm) and

with good signal-to-noise ratio were chosen to generate reference spectra. For polydisperse particles generated in the AIDA chamber, the corresponding average spectra include particles of broader size distributions compared to those preselected by the DMA. Information on particle generation or source as well as the sizes is listed in Table 1.

A qualitative comparison between the relative peak intensity ratios within an single particle spectrum and those in another spectrum can yield relative quantitation information, as suggested by Gross et al. (2000). We add information on typical peak ratios to some of our reference spectra to help identify specific species.

3.2.1 Pure compound particles

Although particles consisting of one single species only are rarely sampled in the atmosphere, interpretation of mass spectra of ambient samples is supported by the knowledge about the mass spectra of pure compounds. In the following mass spectra for a few typical ambient aerosol constituents are discussed.

Figure 3 shows average spectra for pure compound aerosol particles. For NH_4NO_3 particles (panel A), we observed the positive ions m/z 18 NH_4^+ and m/z 30 NO^+; and the negative ions m/z 46 NO_2^- and m/z 62 NO_3, similar to Reitz et al. (2016). The LAAPTOF is much less sensitive to ammonium than nitrate fragments, leading to a weak NH_4^+ signal and prominent NO^+, NO_2^- and NO_3^- peaks. The ratio of NO^+ to NH_4^+ is ~48, and the ratio of NO_2^- to NO_3^- is ~4. The prominent peak of NO^+ arises not only from nitrate (majority), but also from ammonium (Murphy et al., 2006). In our ammonium nitrate spectra, there are weaker signatures of m/z 46 NO_2^+ and m/z 125 $HNO_3{\cdot}NO_3^-$ (not shown here, but visible and reproducible), which were also observed in PALMS mass spectra (Zawadowicz et al., 2015). For K_2SO_4 particles, we observed the potassium signals at m/z 39 K^+ and m/z 41 K^+, and a sulphate signature with ion clusters grouped around m/z 32 S^-, m/z 64 SO_2^-, m/z 80 SO_3^- and m/z 96 SO_4^-. Note that the extra peak at m/z 40^+ besides m/z 39 K^+ in Fig. 3 (B) is likely due to the incorrect mass assignments as a result of peak shifts (refer to section 2.5 and "Procedure 1" in the supplementary information). For high-intensity peaks such as sodium chloride NaCl, extra peaks next to the main peak (Fig. S3) may have an additional reason: "Ringing" due to partial saturation of the data acquisition system or signal reflections within the data acquisition circuitry (Gross et al., 2000). The real intensities of m/z 35 Cl^- should include its corresponding side ringing peak. For the ratio of m/z 39 K^+ to m/z 41 K^+ is ~13.2, close to the natural isotopic ratio of ~13.9 for $^{39}K/^{41}K$. For pure NaCl particles, the ratio of m/z 35 Cl^- to m/z 37 Cl^- is ~3.2, similar to the natural isotopic ratio of ~3.1 for $^{35}Cl/^{37}Cl$. Therefore, these two isotopic ratios can be used as markers to identify K and Cl measured by LAAPTOF. Another inorganic compound measured here is silica (Fig. S4) and its typical peak ratio of (m/z 76 SiO_3^- + m/z 77 $HSiO_3^-$) to m/z 60 SiO_2^- is ~1.0. The corresponding histograms of such ratios for different particle samples can be found in Fig. S5.

High signal intensities in oxalic acid spectra are observed at m/z 18 H_2O^+, 28 CO^+, and 30 CH_2O^+, as well as some weaker peaks at m/z 40^+, 44^+, 56^+, and 57^+. M/z 89 $C_2O_4H^-$ is used as signature ion for oxalic acid in other SPMS studies (Roth et al., 2016). In our study, a distinct signal at around m/z 89^- is observed as well, indicating oxalate fragment formation after laser ablation.

In order to identify humic like substances in the ambient particles, we measured humic acid particles (Fig. S6) and found hydrocarbon and elemental carbon fragments, with very prominent peaks at m/z 24^-, 25^-, and 26^- suggested to be organic ions (Silva et al., 2000), as well as peaks at m/z 25^-, 26^-, 49^-, and 73^- for unsaturated organic compounds.

3.2.2 Particles consisting of well-defined internal mixtures

Figure 4 shows average spectra from homogeneously internally mixed particles. The spectrum from the mixture of NH_4NO_3 and $(NH_4)_2SO_4$ (panel A) contains the signature from pure NH_4NO_3 particles, but with lower relative intensities (each peak intensity

is normalized to the sum of ion signal) for NO_2^- and NO_3^-, due to the formation of anion clusters at ~m/z=80 SO_3^- and 97 HSO_4^-. Compared to the pure NH_4NO_3 particles, the ratio of NO^+ to NH_4^+ (~34) is ~30% lower in the spectrum for the mixture, due to its lower molar ratio of nitrate/ammonium, whereas the ratio of NO_2^- to NO_3^- (~7) is 80% higher. In addition, as already discussed in section 3.1.2, the better UV light absorber NH_4NO_3 assists in light absorbing for mixed particles, resulting in a sulphate signature that could not be observed for pure $(NH_4)_2SO_4$. This exemplifies potential effects of individual particle chemical composition on mass spectral performance of the LAAPTOF. For the mixture of K_2SO_4 and NaCl (panel B), similar signatures as for the pure particles were observed. Compared to the pure NaCl particle spectra, the signal intensity of Na^+ is decreased. This can be explained by more cations formed from the mixed particles, including from potassium, which has a higher ionization potential and lower lattice energy than NaCl. For the mixed particles, expected clusters such as 113/115 K_2Cl^+, 109 KCl_2^-, and 119 $NaSO_4^-$ and a minor fragment 97 $KNaCl^+$ were observed, but not 81/83 Na_2Cl^+ as found in pure NaCl particles. These results show that compared to pure compounds, mass spectra from aerosol particles consisting of mixtures can feature new ions, while some marker ions for the pure compounds may disappear. These spectra are thus not simply a combination of the spectra from single component particles. Another example for an inorganic mixture of NH_4NO_3 and K_2SO_4 is provided in Fig. S7. The α-pinene SOA spectrum is shown in panel (C) of Fig. 4. Ablation of α-pinene SOA particles forms different types of organic fragments: 1) hydrocarbon and oxygenated organic fragments $C_xH_yO_z$, (x=1–6, y=0–9, z=0–3, details about the peak assignments can be found in Table S1), except for m/z 59^+, 83^+, 85^+, and 95^+, are comparable to the combination mass spectral patterns for cis-pinonic and pinic acids (refer to Fig. S8) which are oxidation products from α-pinene ozonolysis (Saathoff et al., 2009; Yu et al., 1999); 2) Carbon clusters 12 C^+, 24 C_2^+, 36 C_3^+, and 60 C_5^+, with the most prominent peak in 12 C^+, assigned to both soot and organic matter fragments in another LAAPTOF study (Ahern et al., 2016); 3) Carboxylic acid groups in the negative spectra, e.g. 45 $COOH^-$, 59 CH_2COOH^-, 73 $C_2H_4COOH^-$, 85 $C_3H_4COOH^-$ and 99 $C_4H_6COOH^-$.

Figure 5 (A) shows the spectrum for heterogeneously internally mixed K_2SO_4 and PSL particles (PSL core, K_2SO_4 shell). All signatures for PSL particles, i.e. hydrocarbon fragments in positive spectra, intensive organic signature m/z 24^-, 25^-, and 26^-, carbon clusters $C_n^{+/-}$, and m/z 49^- and 73^- fragments arising from unsaturated structures such as aromatic structures are retained in this spectra (grey labels), and the corresponding peak intensities are similar to the pure PSL particles (Fig. S9). However, the intensities of most of the K_2SO_4 fragments are weaker compared to pure K_2SO_4 particles, likely due to the quite thin or only partial coating layer of K_2SO_4 on the PSL core (the nominal geometric size of the PSL particles mixed with the aqueous solution of K_2SO_4 was 800 nm which is the same size that was selected by the DMA prior to sampling by the mass spectrometer.). The most prominent peak at m/z 39^+ with a normalized intensity of ~0.46, containing both K^+ and $C_3H_3^+$ fragments, is mainly attributed to K^+ (intensity ~0.73 for pure K_2SO_4), since the intensity of $C_3H_3^+$ (~0.06) for pure PSL is much lower (refer to Fig. S9). The still intensive signal from 39 K^+ despite the weaker sulphate peaks corresponds to the high sensitivity of the instrument for potassium. Fig. 5 (B) shows the average spectrum for poly(allylamine hydrochloride) coated gold particles. Prominent signatures of nitrogen containing compounds (NOCs) are observed at m/z 58 C_2H_5-NH-CH_2^+, 15 NH^+, 26 CN^-, and 42 CNO^-, as well as the signatures for unsaturated organic compounds at m/z 25^-, 26^-, 49^-, and 73^-. Strong intensities for m/z (35^- plus 36^-) and 37^- with ratio a of ~3.1 can be assigned to Cl isotopes derived from the hydrochloride. We also observed small gold peaks at m/z $197^{+/-}$ both in positive and negative spectra.

Mass spectra for other well-defined compounds, i.e. synthetic hematite and pure sea salt particles, are also provided in the supplementary information (Fig. S10 and S11).

3.2.3 Particles consisting of complex mixtures

Figure 6 shows the average spectra for different types of soot particles. All of them show characteristic patterns for elemental carbon (EC) $Cn^{+/-}$. For soot1 with high organic carbon (OC) content from propane combustion in the laboratory (panel B), prominent peaks were observed at m/z 28 CO^+ and 27 $C_2H_3^+$, as well as some other organic carbon signatures at m/z 39^+, 40^+, 44^+ and 56^+. All the organic signatures in soot1 with high OC were also observed for soot3, lignocellulosic char from chestnut wood (panel D), indicating that biomass burning soot contains a significant fraction of OC. It should be noted that biomass burning will also form potassium, thus m/z 39^+ contains both K^+ and $C_3H_3^+$ fragments. M/z 24^-, 25^- and 26^- can be observed in all the soot types, but with a bit different patterns: 1) soot with high EC content shows very high m/z 24^- (~2 to 3 times than m/z 25^-), while 2) soot with high OC shows comparable or even higher m/z 25^- to/than m/z 24^-. These patterns might provide help to distinguish EC and OC contributions in the spectra from ambient particles.

Figure 7 shows spectra for Arizona test dust (milled desert dust) (panel A), arable soil SDGe01 sampled from Gottesgabe in Germany (B), and agricultural soil dust collected from harvesting machines after rye and wheat harvest (C). For Arizona test dust, we observed high mineral signatures of aluminium and silicon containing clusters, namely 27 Al^+, 28 Si^+, 44 SiO^+, 43 AlO^-, 59 AlO_2^-, 60 SiO_2^-, 76 SiO_3^-, 119 $AlSiO_4^-$, 179 $AlSiO_4.SiO_2^-$, 136 $(SiO_2)_2O^-$. It should be noted that high 16 O^- and 17 OH^- accompany the intensive mineral signatures, attributed to the adsorbed water on the active surface of mineral particles. In spectra (A), we also observed the following peaks: other mineral related metal clusters, e.g. 7 Li^+, 23 Na^+, 24 Mg^+, 40 Ca^+, 39/41 K^+, 55 Mn^+, 56 Fe^+, 58 Ni^+, 64 Cu^+, metal oxides and hydroxides, e.g. 56 CaO^+, 57 $CaOH^+$, 96 Ca_2O^+, 112 $(CaO)_2^+$, and 88 FeO_2^-, as well as weak anion clusters of organic signature (m/z 24 C_2^-, 25 C_2H^-, 26 $C_2H_2^-$, and 42 $C_2H_2O^-$), NOCs (m/z 26 CN^- and 42 CNO^-), chloride (m/z 35^- and 37^-), sulphate (m/z 32^-, 48^-, 64^-, 80^-, and 97^-), phosphate (63 PO_2^- and 79 PO_3^-), diacids (oxalate 89 $(CO)_2OOH^-$ and 117$(CO)_3OOH^-$) and an unknown fragment m/z 148^-. M/z 26^+ in panels (B) and (C) is much higher than m/z 24^- and 25^-, due to the contribution of CN fragments from NOCs. Similar signatures can also be observed in the spectra for Saharan desert dust (Fig. S12).

Most of the mineral and organic fragments of soil dust are similar to those of desert dust, however with different intensities, e.g. m/z 24^-, 25^-, 26^-, and 42^- (labelled in green) are more intensive than those in desert dust, indicating higher organic compound content. Some peak ratios of fragments are similar across the different dust types, e.g. 40 Ca^+ to 56 CaO^+ is 2.2, 1.1, and 2 for desert dust, arable soil dust and agricultural soil dust, respectively. Compared with desert dust, there are different fragments from soil dust particles, e.g. EC patterns (labelled in grey), organic acids signatures (blue), ammonium signatures (orange), unsaturated organic fragments (m/z 49^- and 73^-) and some other unknown fragments (Weimer et al.). For arable soil dust particles, we also measured samples from Paulinenaue in Germany (SDPA01), Argentina (SDAr08) and Wyoming in USA (SDWY01) (refer to Fig. S13). Dominant mass spectral peak patterns are similar across all soil dust samples. They are located at around m/z 27^+, 39^+, and 56^+ in the positive spectra; and 26^-, 42^-, 60^-, and 76^- in negative spectra. Less prominent but reproducibly detected are carboxylic acid groups (e.g. $COOH^-$) and EC patterns. The German soil dust, however, contains more organic species than soil dust from Argentina and USA, reflected in higher intensities at m/z 24^-, 25^-, and 26^-. Argentinian soil dust contains much less mineral species, expressed in much lower intensities of mineral signatures, e.g. m/z 27^+, 28^+, 40^+, 44^+, and 56^+. The ratios of m/z 39 K^+ and 41 K^+ (3.6, 3.8, 3.5, 5.3 for SDGe01, SDPA01, SDAr08, and SDWY01, respectively) are much lower than the typical peak ratio (~10.6) for potassium (Table 2), indicating that they are likely contributed to by both potassium isotopes and hydrocarbon fragments.

For agricultural soil dust particles, obviously ammonium (m/z 18 NH_4^+ and 30 NO^+), phosphate (m/z 63 PO_2^-, 79 PO_3^-, and 95 PO_5^-) and potassium signatures (m/z 39 K^+ and 41 K^+) can be found in the spectra, attributed to fertilization. Apart from that, typical biological signatures were observed: 1) the strong m/z 26^-, 42^-, and 39^+ pattern is similar to the potassium organo-nitrogen particle type observed by an ATOFMS at an urban site in Barcelona (Dall'Osto et al., 2016), and which were assigned to

carbohydrates, arising from biogenic species (Schmidt et al., 2017; Silva et al., 2000). 2) 26^- and 42^- could also be contributed by CN^- and CNO^- derived from NOCs, i.e. amines, as well as m/z 30 CH_3NH^+, 58 $C_2H_5NHCH_2^+$, and 59 $(CH_3)_3N^+$. These biological signatures have also been observed by ALABAMA in the field (Schmidt et al., 2017). 3) Some weak but reproducibly detected fragment pattern at around m/z 77 $C_6H_5^+$, 91 $C_7H_7^+$, 103 $C_8H_7^+$, 105 $C_8H_9^+$, and 115 $C_9H_7^+$ might be originate from aromatic compounds. Similar patterns can also be found for PSL particles.

Other examples for complex mixtures, i.e. illite and sea salt particles with biological components are provided in the supplementary information (Fig. S14 and S11).

All the peak assignments and mass spectral patterns like signature peaks as well as some stable peak ratios mentioned above have been summarized in Table S1 and Table 2, respectively. We consider these laboratory-based reference spectra as useful for the analysis of data obtained also by other LAAPTOF versions and to some extend even for other single particle mass spectrometers. Similar mass spectra are to be expected as long as they use similar ablation & ionization laser pulses (4 mJ, 193 nm), inlet regions for the mass spectrometer, and mass spectrometer types. In the near future, we plan to make these laboratory-based reference spectra publicly available via the EUROCHAMP-2020 data base (www.eurochamp.org).

3.3 Interpretation of field data

Figure 8 shows an example of bipolar mass spectra for six different particle classes measured in the field campaign at a rural site near Leopoldshafen in southwest Germany. On July 29th, 2016 within 24 hours, 7314 particles were detected, successfully ablated and mass spectra generated by LAAPTOF. The 7314 pairs of spectra were then clustered by the Fuzzy c-means algorithm, resulting in six classes. The resulting number of classes with clearly different features depends on the experience of the operating scientist to identify them (please refer to the details of Fuzzy clustering in Procedure 1 in the supplementary information). The Fuzzy results are compared with the laboratory-based reference spectra by calculating their correlation coefficients (Fig. 9). All classes exhibit a sulphate signature with m/z 97 HSO_4^- and m/z 80 SO_3^-; a nitrate signature with m/z 46 NO_2^- and 62 NO_3^-; an organic compound signature with m/z 24 C_2^-, 25 C_2H^-, and 26 C_2H_2/CN^-; and a NOC signature with m/z 26 CN^- and 42 CNO^- in the negative spectra. More characteristic signatures for each particle class can be observed in the positive spectra. All particles measured on this day show a 35% similarity to class 5 with obvious signatures for potassium (K) and sulphate, with significant correlation with the reference particles containing potassium and sulphate (Fig. 9). Besides, class 5 also has significant correlation with some other cations arising from ammonium, organic compounds, and dust. The ratio of m/z (39^+ + 40^+) to 41^+ is ~11, close to the value for pure K_2SO_4 particles (~13.5), thus we assigned them to K^+ rather than organic fragments. Further, there is a 15% similarity to class 4 with prominent ammonium signatures at m/z 18 NH_4^+ and 30 NO^+, sulphate signatures, as well as a relatively weaker but reproducible nitrate signature. The corresponding spectrum is similar as the spectrum for the homogeneous mixtures of NH_4NO_3 and $(NH_4)_2SO_4$ (panel A in Fig. 4). This class also has strong correlation with both positive and negative reference spectra for the mixture of ammonium nitrate and ammonium sulphate particles. Ammonium, nitrate and sulphate are the major secondary inorganic species in atmospheric aerosol particles (Seinfeld and Pandis, 2006), thus we name this class "secondary inorganic". It should be noted that this class has significant correlation with ammonium and cations arising from oxalic acid, however class 4 has weak correlation with the signature cation, i.e. m/z 89 $C_2O_4H^-$ (oxalate), of oxalic acid. Therefore, we can rule out a significant contribution of oxalic acid. There is also a 15% similarity to class 2 (sodium rich), with a characteristic pattern of a strong signal at m/z 23 Na^+ accompanied by two weaker peaks at m/z 39 K^+ (with typical potassium peak ratio of ~12) and 63^+ (might contain both Cu^+ and $C_5H_3^+$ fragments). Class 2 has significant correlation with the cations (i.e. Na and K) arising from sea salt, but weak correlation with its anions, such as m/z 35^- and 37^- chloride isotopes. A sea salt contribution can thus be ruled out. Its negative spectrum significantly correlates with nitrate,

sulphate, and dust particles. Besides sodium rich dust aged sea salt may be an appropriate classification. Class 3 is named "aged soot", since it has significant correlation with soot particles, especially diesel soot, and a prominent sulphate signal. This class has an EC pattern with m/z 12n C_n^+, similar to those in the reference spectra for soot particles (Fig. 6) as well as the reference spectra for PSL particles (Fig. S9). The patterns at m/z 27 $C_2H_3^+$ and 28 CO^+, m/z 36 C_3^+ and 39 $C_3H_3^+$ as well as the m/z 24^-, 25^- and 26^- with higher m/z 26^-, indicate an OC contribution. This is supported by the correlations especially with PSL particles but also several other organic compounds, suggesting that this class of particles contains organic species. Class 6 is dominated by calcium (Ca) and sulphate with characteristic calcium signature peaks at m/z 40 Ca^+ and 56 CaO^-, also found in the spectra for dust particles (Fig. 7, Fig. S12, and S13). M/z 40^+ and 56^+ may also contain 40 C_2O^+ and 56 $Fe/C_4H_8^+$ fragments, respectively. Class 1 contains almost all fragments observed in other classes, and is thus named "more aged /mixed particles". As shown in Fig. 9, class 6 is consequently correlated with almost all of the reference spectra (both positive and negative ones).

In order to further interpret the field data, we also classified the ambient mass spectra only based on correlation with 17 selected laboratory-based reference spectra (10 positive + 7 negative spectra) listed in Table S2. This approach resulted in 13 particle types, 7 more than were distinguished by Fuzzy clustering. It should be mentioned that at the beginning we were able to identify all but the Ca rich particle class resulting from Fuzzy clustering, since initially we did not have a reference for this type. We therefore used class 6 as an additional reference spectrum for this type of particles, which is among one of the 13 types (here we use "types" instead of "classes" in order to differentiate these two classification methods). Their corresponding spectra are shown in Fig. 10. All the types above the dashed line (A to I) exhibit more prominent secondary inorganic signatures (m/z 97 HSO_4^-) and higher number fractions than the ones below the dashed line. Although particle types A-I all exhibit a more prominent sulphate pattern with m/z 80 and 97 than nitrate pattern with m/z 46 and 62, they are higher correlated with the mixture of nitrate and sulphate than either of them. Therefore, we assign the corresponding types to nitrate and sulphate. All the types in the lower panels (J to M) have significant correlation with arable soil dust in the negative spectra, which have organic signatures, e.g. m/z 24^-, 25^-, and 26^-, as well as some mineral signatures like m/z 119^-. Compared with the negative spectra, the positive spectra are more characteristic, which was also observed in the Fuzzy results. Type A, B, C, D, and E are comparable with Fuzzy class 5, 4, 2, 6, and 3, respectively (the correlation coefficients are 0.89 for type A and class 5, 0.95 for type B and class 4, 0.84 for type C and class 2, 0.76 for type D and class 6, and 0.81 for type E and class 3). Types F to I are more similar to aged/mixed particles, with more fragments compared to types A to E. Type H is comparable with Fuzzy class 1. About 10% of the particles cannot be grouped into any type. This is most likely because of an incorrect mass assignment for the stick spectra, resulting from too large spectrum-to-spectrum peak shifts for the same ion fragments/clusters which cannot be corrected on a single particle basis with the existing software (Ramisetty et al., 2017). As shown in the spectra in both Fig. 8 and 10, all organic species were internally mixed with inorganic species.

This reference spectra based classification can also be used for identification of particles with low number fractions among the huge amount of ambient data, and for selection of particles containing particular species e.g. for which the instrument has a lower sensitivity. This can be achieved by e.g. excluding peaks with high signal such as m/z 39 $K/C_3H_3^+$, or selecting a certain particle size range, or mass range. As an example, 55 lead containing particles (Pb, with isotopes at m/z 206, 207, and 208) (details are given in the Procedure 3 in the supplementary information) were identified among the 7314 ambient aerosol particles. The resulting spectra of particle classes/types in one field study can also be used as reference for other studies. More applications of these procedures for field data interpretation will be presented in an upcoming paper.

In short, Fuzzy and reference spectra based classifications have some comparable results with high correlations (r: 0.76–0.95) and also have different advantages: Fuzzy classification can identify special ambient particle types without any existing reference if they have a significant abundance and signal strength, while reference spectra-based methods can identify target particle types

even with little abundance. They are complementary to some extend and thus their combination has the potential to improve interpretation of field data.

4 Conclusions

In this study, the overall detection efficiency (ODE) of LAAPTOF was determined to range from ~(0.01 ± 0.01)% to ~(4.23 ± 2.36)% for polystyrene latex (PSL) with the size of 200 to 2000 nm, ~(0.44 ± 0.19)% to ~(6.57 ± 2.38)% for ammonium nitrate (NH_4NO_3) and ~(0.14 ± 0.02)% to ~(1.46 ± 0.08)% for sodium chloride (NaCl) particles in the size rage of 300 to 1000 nm. This is a relative good detection efficiency compared to earlier versions of the instruments especially when considering the good reproducibility and stability even during field measurements. A comparison to other single particle mass spectrometers is subject of another study and will be discussed in a separate publication. Matrix effects from aerosol particles (e.g. size, morphology and optical property) and certain instrument influences (e.g. aerodynamic lens, detection system) and their interaction must be taken into account to evaluate the LAAPTOF performance.

In order to facilitate the interpretation of single particle mass spectra from field measurements, we have measured various well defined atmospherically relevant aerosol particles in the laboratory and provide here laboratory-based reference spectra for aerosol particles of different complexity with comprehensive spectral information about the components (such as organic compounds, elemental carbon, sulphate, nitrate, ammonium, chloride, mineral compounds, metals, etc. as commonly observed in atmospheric aerosol particles). Our results show that the interpretation of spectra from unknown particle types is significantly supported by using known mass spectral patterns like signature peaks for ammonium, nitrate, sulphate, and organic compounds as well as typical peak ratios for e.g. potassium, silicon, and chlorides. Spectra for internally mixed particles may show new clusters of ions, rather than simply a combination of the ions from single component particles. This may be a complication for data interpretation which can be overcome if suitable reference spectra for correspondingly mixed particles are available. Organic compounds generally have some ions in common but exhibit variations depending on the compound. Several peaks can originate from different fragments: for example, m/z 26^- and 42^- could be CN^- and CNO^- and/or $C_2H_2^-$ and $C_2H_2O^-$, m/z 39^+ and 41^+ could originate from K^+ isotopes or organic fragments, and organic matter can also be ionized to form the typical elemental carbon pattern with $C_n^{+/-}$ ions. Hence the interpretation is not always unambiguously possible for such particles but may require additional information (e.g. size, additional marker peaks, or even higher resolution spectra) or comparison to data from other instruments like on-line aerosol mass spectrometers (e.g. AMS) or chemical ionization mass spectrometers (e.g. FIGAERO-CIMS).

A set of 7314 mass spectra obtained during one day of field measurements was used for particle type classification by both Fuzzy clustering and reference spectra. Fuzzy clustering-yielded six different classes, which could then be identified with the help of reference spectra. Classification of the mass spectra based on comparison with 17 reference spectra resulted in 13 different particle types, six of which exhibited high correlation with the Fuzzy clusters (r: 0.76–0.95). Compared with the reference spectra, we found that each particle class/type has a sulphate signature at m/z 80 SO_3^- and 97 HSO_4^-, a nitrate signature at m/z 46 NO_2^- and 62 NO_3^-, an organic compound signature at m/z 24 C_2^-, 25 C_2H^- and 26 C_2H_2/CN^- and a nitrogen-containing organic signature at m/z 26 CN^- and 42 CNO^-. Furthermore, we performed a target-oriented classification by using selected reference spectra, allowing for the identification of particles with low number fraction in the ambient aerosol, e.g. lead-containing particles. Based on our results we advise using a combination of both methods for the analysis of SPMS field data.

We conclude that the reference spectra presented in this paper are useful for interpretation of field measurements and for understanding the impact of mixing on typical mass spectral signatures. Furthermore, the reference spectra should be useful for

interpretation of data obtained by other LAAPTOF versions or other single particle mass spectrometers using a similar ionization method and comparable mass spectrometers. For future experiments using the LAAPTOF, systematic studies on its sensitivity to different species, distinguishing the organic and inorganic contribution to the same peak in the spectra, and investigating peak ratios are still required.

Data availability

The reference spectra are available upon request from the authors and will be made available in electronic format via the EUROCHAMP-2020 data base (www.eurochamp.org).

Author contributions

X.S. characterised the LAAPTOF, measured all the particles samples, did the data analysis, produced all figures, and wrote the manuscript. R.R. helped to characterise the LAAPTOF and to measure some of the particle samples. C.M. provided technical and scientific support for characterising the LAAPTOF as well as data analysis, and for interpretation and discussion of the results. W.H. provided scientific support for interpretation and discussion of the results. T.L. gave general advices and comments for this paper. H.S. provided technical and scientific support for characterising the LAAPTOF, as well as suggestions for the data analysis, interpretation and discussion. All authors contributed to the final text.

Competing interests

The authors declare that they have no conflicts of interest.

Acknowledgements

The authors gratefully thank the AIDA staff at KIT for helpful discussions and technical support, and the China Scholarship Council (CSC) for financial support of Xiaoli Shen and Wei Huang. Special thanks go to Robert Wagner for Mie calculation and discussion and comments on the sea salt samples, to Thea Schiebel, Kristina Höhler, and Ottmar Möhler for discussions about the soil dust samples, to Isabelle Steinke for discussions regarding the plant samples, to Konrad Kandler for providing the Morocco desert dust samples, to Roger Funk and Thomas Hill for providing the soil dust samples, to Elena Gorokhova and Matt Salter for providing the sea salt with skeletonema marinoi culture, and to Aeromegt GmbH for discussions about the LAAPTOF performance and analysis software.

References

Ackerman, A. A., Adam, J. A., Cairns, B., Cho, H., Gritsevich, M., Jethva, H., Kacenelenbogen, M., Kandler, K., Knobelspiesse, K., Lanconelli, C., Lupi, A., Mazzola, M., Nousiainen, T., Peltoniemi, J. I., Platnick, S., Puttonen, E., Savenkov, S. N., Segal-Rosenheimer, M., Sharma, S., Tomasi, C., Torres, O., and Zhang, Z.: Light scattering reviews 9: Light scattering and radiative transfer, Springer-Praxis, 2015.

Ahern, A. T., Subramanian, R., Saliba, G., Lipsky, E. M., Donahue, N. M., and Sullivan, R. C.: Effect of secondary organic aerosol coating thickness on the real-time detection and characterization of biomass-burning soot by two particle mass spectrometers, Atmos Meas Tech, 9, 6117–6137, 2016.

Arndt, J., Sciare, J., Mallet, M., Roberts, G. C., Marchand, N., Sartelet, K., Sellegri, K., Dulac, F., Healy, R. M., and Wenger, J. C.: Sources and mixing state of summertime background aerosol in the northwestern Mediterranean basin, Atmos Chem Phys, 17, 6975–7001, 2016.

Bohren, C. F. and Huffman, R. D.: Absorption and scattering of light by small particles, WILEY-VCH Verlag GmbH & Co. KGaA, 2007.

Brands, M., Kamphus, M., Böttger, T., Schneider, J., Drewnick, F., Roth, A., Curtius, J., Voigt, C., Borbon, A., Beekmann, M., Bourdon, A., Perrin, T., and Borrmann, S.: Characterization of a newly developed aircraft-based laser ablation aerosol mass spectrometer (ALABAMA) and first field deployment in urban pollution plumes over Paris during MEGAPOLI 2009, Aerosol Sci Tech, 45, 46–64, 2011.

Burkholder, J. B., Abbatt, J. P. D., Barnes, I., Roberts, J. M., Melamed, M. L., Ammann, M., Bertram, A. K., Cappa, C. D., Carlton, A. G., Carpenter, L. J., Crowley, J. N., Dubowski, Y., George, C., Heard, D. E., Herrmann, H., Keutsch, F. N., Kroll, J. H., McNeill, V. F., Ng, N. L., Nizkorodov, S. A., Orlando, J. J., Percival, C. J., Picquet-Varrault, B., Rudich, Y., Seakins, P. W., Surratt, J. D., Tanimoto, H., Thornton, J. A., Tong, Z., S., T. G., Wahner, A., Weschler, C. J., Wilson, K. R., and Ziemann, P. J.: The essential role for laboratory studies in atmospheric chemistry, Environ Sci Technol, 51, 2519–2528, 2017.

Canagaratna, M. R., Jayne, J. T., Jimenez, J. L., Allan, J. D., Alfarra, M. R., Zhang, Q., Onasch, T. B., Drewnick, F., Coe, H., Middlebrook, A., Delia, A., Williams, L. R., Trimborn, A. M., Northway, M. J., DeCarlo, P. F., Kolb, C. E., Davidovits, P., and Worsnop, D. R.: Chemical and microphysical characterization of ambient aerosols with the aerodyne aerosol mass spectrometer, Mass Spectrom Rev, 26, 185–222, 2007.

Dall'Osto, M., Beddows, D. C. S., McGillicuddy, E. J., Esser-Gietl, J. K., Harrison, R. M., and Wenger, J. C.: On the simultaneous deployment of two single-particle mass spectrometers at an urban background and a roadside site during SAPUSS, Atmos Chem Phys, 16, 9693–9710, 2016.

Gaie-Levrel, F., Perrier, S., Perraudin, E., Stoll, C., Grand, N., and Schwell, M.: Development and characterization of a single particle laser ablation mass spectrometer (SPLAM) for organic aerosol studies, Atmos Meas Tech, 5, 225–241, 2012.

Gemayel, R., Hellebust, S., Temime-Roussel, B., Hayeck, N., Van Elteren, J. T., Wortham, H., and Gligorovski, S.: The performance and the characterization of laser ablation aerosol particle time-of-flight mass spectrometry (LAAP-ToF-MS), Atmos Meas Tech, 9, 1947–1959, 2016.

Gross, D. S., Gälli, M. E., Silva, P. J., and Prather, K. A.: Relative sensitivity factors for alkali metal and ammonium cations in single particle aerosol time-of-flight mass spectra, Anal Chem, 72, 416–422, 2000.

Hagemann, R., Corsmeier, U., Kottmeier, C., Rinke, R., Wieser, A., and Vogel, B.: Spatial variability of particle number concentrations and NOx in the Karlsruhe (Germany) area obtained with the. mobile laboratory 'AERO-TRAM', Atmos Environ, 94, 341–352, 2014.

Hinz, K. P., Greweling, M., Drews, F., and Spengler, B.: Data processing in on-line laser mass spectrometry of inorganic, organic, or biological airborne particles, J Am Soc Mass Spectr, 10, 648–660, 1999.

Jimenez, J. L., Canagaratna, M. R., Donahue, N. M., Prevot, A. S. H., Zhang, Q., Kroll, J. H., DeCarlo, P. F., Allan, J. D., Coe, H., Ng, N. L., Aiken, A. C., Docherty, K. S., Ulbrich, I. M., Grieshop, A. P., Robinson, A. L., Duplissy, J., Smith, J. D., Wilson, K. R., Lanz, V. A., Hueglin, C., Sun, Y. L., Tian, J., Laaksonen, A., Raatikainen, T., Rautiainen, J., Vaattovaara, P., Ehn, M., Kulmala, M., Tomlinson, J. M., Collins, D. R., Cubison, M. J., Dunlea, E. J., Huffman, J. A., Onasch, T. B., Alfarra, M. R., Williams, P. I., Bower, K., Kondo, Y., Schneider, J., Drewnick, F., Borrmann, S., Weimer, S., Demerjian, K., Salcedo, D., Cottrell, L., Griffin, R., Takami, A., Miyoshi, T., Hatakeyama, S., Shimono, A., Sun, J. Y., Zhang, Y. M., Dzepina, K., Kimmel, J. R., Sueper, D., Jayne, J. T., Herndon, S. C., Trimborn, A. M., Williams, L. R., Wood, E. C., Middlebrook, A. M., Kolb, C. E., Baltensperger, U., and Worsnop, D. R.: Evolution of organic aerosols in the atmosphere, Science, 326, 1525–1529, 2009.

Johnston, M. V.: Sampling and analysis of individual particles by aerosol mass spectrometry, J Mass Spectrom, 35, 585–595, 2000.

Kamphus, M., Ettner-Mahl, M., Brands, M., Curtius, J., Drewnick, F., and Borrmann, S.: Comparison of two aerodynamic lenses as an inlet for a single particle laser ablation mass spectrometer, Aerosol Sci Tech, 42, 970–980, 2008.

Kulkarni, P., Baron, P. A., and Willeke, K.: Aerosol measurement: Principles,techniques, and applications, Wiley, J & Sons, Inc., 2011.

Li, L., Huang, Z. X., Dong, J. G., Li, M., Gao, W., Nian, H. Q., Fu, Z., Zhang, G. H., Bi, X. H., Cheng, P., and Zhou, Z.: Real time bipolar time-of-flight mass spectrometer for analyzing single aerosol particles, Int J Mass Spectrom, 303, 118–124, 2011.

Li, W., Sun, J., Xu, l., Shi, Z., Riemer, N., Sun, Y., Fu, P., Zhang, J., Lin, Y., Wang, X., Shao, L., Chen, J., Zhang, X., Wang, Z., and Wang, W.: A conceptual framework for mixing structures in individual aerosol particles, J Geophys Res-Atmos, 121, 13784–13798, 2016.

Lin, Q. H., Zhang, G. H., Peng, L., Bi, X. H., Wang, X. M., Brechtel, F. J., Li, M., Chen, D. H., Peng, P. A., Sheng, G. Y., and Zhou, Z.: In situ chemical composition measurement of individual cloud residue particles at a mountain site, southern China, Atmos Chem Phys, 17, 8473–8488, 2017.

Liu, P., Ziemann, P. J., Kittelson, D. B., and McMurry, P. H.: Generating particle beams of controlled dimensions and divergence: II. Experimental evaluation of particle motion in aerodynamic lenses and nozzle expansions, Aerosol Sci Tech, 22, 314–324, 1995.

Marsden, N. A., Flynn, M. J., Allan, J. D., and Coe, H.: On-line dfferentiation of mineral phase in aerosol particles by ion formation mechanism using a LAAP-TOF single particle mass spectrometer, Atmos Meas Tech, 11, 195–213, 2018.

Marsden, N. A., Flynn, M. J., Taylor, J. W., Allan, J. D., and Coe, H.: Evaluating the influence of laser wavelength and detection stage geometry on optical detection efficiency in a single-particle mass spectrometer, Atmos Meas Tech, 9, 6051–6068, 2016.

Moffet, R. C., de Foy, B., Molina, L. T., Molina, M. J., and Prather, K. A.: Measurement of ambient aerosols in northern Mexico City by single particle mass spectrometry, Atmos Chem Phys, 8, 4499–4516, 2008.

Murphy, D. M.: The design of single particle laser mass spectrometers, Mass Spectrom Rev, 26, 150–165, 2007.

Murphy, D. M., Cziczo, D. J., Froyd, K. D., Hudson, P. K., Matthew, B. M., Middlebrook, A. M., Peltier, R. E., Sullivan, A., Thomson, D. S., and Weber, R. J.: Single-particle mass spectrometry of tropospheric aerosol particles, J Geophys Res-Atmos, 111, 2006.

Murphy, D. M., Middlebrook, A. M., and Warshawsky, M.: Cluster analysis of data from the Particle Analysis by Laser Mass Spectrometry (PALMS) instrument, Aerosol Sci Tech, 37, 382–391, 2003.

Noble, C. A. and Prather, K. A.: Real-time single particle mass spectrometry: a historical review of a quarter century of the chemical analysis of aerosols, Mass Spectrom Rev, 19, 248–274, 2000.

Pöschl, U.: Atmospheric aerosols: Composition, transformation, climate and health effects, Angew Chem Int Edit, 44, 7520–7540, 2005.

Pratt, K. A. and Prather, K. A.: Mass spectrometry of atmospheric aerosols-Recent developments and applications. Part II: On-line mass spectrometry techniques, Mass Spectrom Rev, 31, 17–48, 2012.

Ramisetty, R., Abdelmonem, A., Shen, X., Saathoff, H., Mohr, C., and Leisner, T.: Exploring femtosecond laser ablation in single particle aerosol mass spectrometry, Atmos Meas Tech Discuss, doi.org/10.5194/amt-2017-357, 2017.

Reitz, P., Zorn, S. R., Trimborn, S. H., and Trimborn, A. M.: A new, powerful technique to analyze single particle aerosol mass spectra using a combination of OPTICS and the fuzzy c-means algorithm, J Aerosol Sci, 98, 1–14, 2016.

Roth, A., Schneider, J., Klimach, T., Mertes, S., van Pinxteren, D., Herrmann, H., and Borrmann, S.: Aerosol properties, source identification, and cloud processing in orographic clouds measured by single particle mass spectrometry on a central European mountain site during HCCT-2010, Atmos Chem Phys, 16, 505–524, 2016.

Saathoff, H., Möhler, O., Schurath, U., Kamm, S., Dippel, B., and Mihelcic, D.: The AIDA soot aerosol characterisation campaign 1999, J Aerosol Sci, 34, 1277–1296, 2003.

Saathoff, H., Naumann, K. H., Möhler, O., Jonsson, A. M., Hallquist, M., Kiendler-Scharr, A., Mentel, T. F., Tillmann, R., and Schurath, U.: Temperature dependence of yields of secondary organic aerosols from the ozonolysis of α-pinene and limonene, Atmos Chem Phys, 9, 1551–1577, 2009.

Schill, G. P. and Tolbert, M. A.: Heterogeneous ice nucleation on phase-separated organic-sulfate particles: effect of liquid vs. glassy coatings, Atmos Chem Phys, 13, 4681–4695, 2013.

Schmidt, S., Schneider, J., Klimach, T., Mertes, S., Schenk, L. P., Curtius, J., and Borrmann, S.: Online single particle analysis of ice particle residuals from mountain-top mixed-phase clouds using laboratory derived particle type assignment, Atmos Chem Phys, 17, 575–594, 2017.

Schreiner, J., Schild, U., Voigt, C., and Mauersberger, K.: Focusing of aerosols into a particle beam at pressures from 10 to 150 Torr, Aerosol Sci Tech, 31, 373–382, 1999.

Seinfeld, J. H. and Pandis, S. N.: Atmospheric chemistry and physics: From air pollution to climate change, Wiley, J & Sons, Inc., Hoboken, New Jersey, 2006.

Silva, P. J., Carlin, R. A., and Prather, K. A.: Single particle analysis of suspended soil dust from Southern California, Atmos Environ, 34, 1811–1820, 2000.

Su, Y. X., Sipin, M. F., Furutani, H., and Prather, K. A.: Development and characterization of an aerosol time-of-flight mass spectrometer with increased detection efficiency, Anal Chem, 76, 712–719, 2004.

Tsigaridis, K., Krol, M., Dentener, F. J., Balkanski, Y., Lathière, J., Metzger, S., Hauglustaine, D. A., and Kanakidou, M.: Change in global aerosol composition since preindustrial times, Atmos Chem Phys, 6, 5143–5162, 2006.

Usher, C. R., Michel, A. E., and Grassian, V. H.: Reactions on mineral dust, Chem Rev, 103, 4883–4939, 2003.

Wagner, R., Kaufmann, J., Möhler, O., Saathoff, H., Schnaiter, M., Ullrich, R., and Leisner, T.: Heterogeneous ice nucleation ability of NaCl and sea salt aerosol particles at cirrus temperatures, J. Geophys. Res. (Atmos.) (in preparation), 2017.

Weimer, M., Schröter, J., Eckstein, J., Deetz, K., Neumaier, M., Fischbeck, G., Hu, L., Millet, D. B., Rieger, D., Vogel, H., Vogel, B., Reddmann, T., Kirner, O., Ruhnke, R., and Braesicke, P.: An emission module for ICON-ART 2.0: implementation and simulations of acetone, Geosci Model Dev, 10, 2471–2494, 2017.

Williams, L. R., Gonzalez, L. A., Peck, J., Trimborn, D., McInnis, J., Farrar, M. R., Moore, K. D., Jayne, J. T., Robinson, W. A., Lewis, D. K., Onasch, T. B., Canagaratna, M. R., Trimborn, A., Timko, M. T., Magoon, G., Deng, R., Tang, D., Blanco, E. D. L. R., Prévôt, A. S. H., Smith, K. A., and Worsnop, D. R.: Characterization of an aerodynamic lens for transmitting particles greater than 1 micrometer in diameter into the Aerodyne aerosol mass spectrometer, Atmos Meas Tech, 6, 3271–3280, 2013.

Wonaschuetz, A., Kallinger, P., Szymanski, W., and Hitzenberger, R.: Chemical composition of radiolytically formed particles using single-particle mass spectrometry, J Aerosol Sci, 113, 242–249, 2017.

Yu, J. Z., Cocker, D. R., Griffin, R. J., Flagan, R. C., and Seinfeld, J. H.: Gas-phase ozone oxidation of monoterpenes: Gaseous and particulate products, J. Atmos. Chem., 34, 207–258, 1999.

Zawadowicz, M. A., Abdelmonem, A., Mohr, C., Saathoff, H., Froyd, K. D., Murphy, D. M., LeisnerI, T., and Cziczo, D. J.: Single-particle time-of-flight mass spectrometry utilizing a femtosecond desorption and ionization laser, Anal Chem, 87, 12221–12229, 2015.

Zawadowicz, M. A., Lance, S., Jayne, J. T., Croteau, P., Worsnop, D. R., Mahrt, F., Leisner, T., and Cziczo, D. J.: Quantifying and improving the performance of the Laser Ablation Aerosol Particle Time of Flight Mass Spectrometer (LAAPToF) instrument, Atmos Meas Tech Discuss, doi: 10.5194/amt-2017-1, 2017.

Zelenyuk, A., Cai, Y., and Imre, D.: From agglomerates of spheres to irregularly shaped particles: Determination of dynamic shape factors from measurements of mobility and vacuum aerodynamic diameters, Aerosol Sci Tech, 40, 197–217, 2006a.

Zelenyuk, A. and Imre, D.: Single particle laser ablation time-of-flight mass spectrometer: An introduction to SPLAT, Aerosol Sci Tech, 39, 554–568, 2005.

Zelenyuk, A., Imre, D., Cai, Y., Mueller, K., Han, Y. P., and Imrich, P.: SpectraMiner, an interactive data mining and visualization software for single particle mass spectroscopy: A laboratory test case, Int J Mass Spectrom, 258, 58–73, 2006b.

Zelenyuk, A., Yang, J., Choi, E., and Imre, D.: SPLAT II: An aircraft compatible, ultra-sensitive, high precision instrument for in-situ characterization of the size and composition of fine and ultrafine particles, Aerosol Sci Tech, 43, 411–424, 2009.

Zhang, Q., Jimenez, J. L., Canagaratna, M. R., Allan, J. D., Coe, H., Ulbrich, I., Alfarra, M. R., Takami, A., Middlebrook, A. M., Sun, Y. L., Dzepina, K., Dunlea, E., Docherty, K., DeCarlo, P. F., Salcedo, D., Onasch, T., Jayne, J. T., Miyoshi, T., Shimono, A., Hatakeyama, S., Takegawa, N., Kondo, Y., Schneider, J., Drewnick, F., Borrmann, S., Weimer, S., Demerjian, K., Williams, P., Bower, K., Bahreini, R., Cottrell, L., Griffin, R. J., Rautiainen, J., Sun, J. Y., Zhang, Y. M., and Worsnop, D. R.: Ubiquity and dominance of oxygenated species in organic aerosols in anthropogenically-influenced Northern Hemisphere midlatitudes, Geophys Res Lett, 34, 2007.

Zhao, W. X., Hopke, P. K., and Prather, K. A.: Comparison of two cluster analysis methods using single particle mass spectra, Atmos Environ, 42, 881–892, 2008.

667 **Table 1: Overview of laboratory generated aerosol particles for reference mass spectra**

Aerosol particle types	Size/nm d_{va}	width[a]	Morphology	Source	Generation method	No. of spectra
1. Particles consisting of pure compounds						
Ammonium nitrate, NH_4NO_3	1160	101	aspherical	≥ 99.5%, Fluka	A	497
Ammonium sulphate[b], $(NH_4)_2SO_4$	611	79	aspherical	≥ 99.5%, Merck	A	537
Potassium sulphate, K_2SO_4	1465	232	aspherical	≥ 99%, Merck	A	300
Sodium chloride, NaCl	1202	133	cubic	≥ 99.5%, Merck	A	250
Silica, SiO_2 (Glass beads)	2097	44	spherical	Palas GmbH	S	347
Oxalic acid, $C_2H_4O_2$	1081	322	spherical	Merck	A	773
Pinic acid, $C_9H_{14}O_4$	902	94	spherical	University of Mainz	A	683
Cis-pinonic acid, $C_{10}H_{16}O_3$	702	88	spherical	98%, ACROS ORGANICS	A	600
Humic acid	1221	126	spherical	100%, Alfa Aesar	A	773
Polystyrene latex (PSL)	818	3	spherical	Thermo scientific	A	235
2. Particles consisting of well-defined mixtures						
Ammonium nitrate & ammonium sulfate (mass ratio = 1:1)	1102	165	aspherical	single component samples are from the same source as the corresponding pure compounds	A	454
Potassium sulfate & sodium chloride (mass ratio = 1:1)	1375	197	aspherical			259
Ammonium nitrate & potassium sulfate (mass ratio = 2:1)	854	112	aspherical			576
Hematite	1091	817	spherical	Karlsruhe Institute of Technology (KIT)	S	320
Pure sea salt	1205	218	cubic	Sigma Aldrich	B1	422
α-Pinene secondary organic aerosols (SOA)	505	84	spherical	(1S)-(-)-α-pinene (99%) from Aldrich	B1[c]	1938
Potassium sulfate coated PSL	805	58	partially coated	Merck & Thermo scientific	A	609
Poly(allylamine hydrochloride) coated gold	400[d]		300 nm core-50 nm shell	Nanopartz Inc.	Nebulized without sizing	417
3. Particles consisting of complex mixtures						
Soot1 with low organic carbon	386[e]	275	agglomerates	incomplete combustion of propane, C/O=0.29	B2	617
Soot1 with high organic carbon	120[e]	58	agglomerates	incomplete combustion of propane, C/O=0.54	B2	347
Soot2 Lignocellulosic char	828	766	agglomerates	Lignocellulosic char from chestnut wood; University of Zürich, Switzerland	S	390
Soot3 Diesel particles	624±980[f]		agglomerates	NIST (2975)	S	533
Arizona test dust	1169	874	aspherical	Powder Technology Inc.	S	261
Saharan desert dust 1 (Morocco)	890	1230	aspherical	Konrad Kandler, TU Darmstadt	S	338
Saharan desert dust 2 (Cairo)	1334±1454[f]		aspherical	Khaled Megahed, KIT	S	396
Arable soil dust SDGe01 (Gottesgabe, Germany)	912	392	aspherical	Roger Funk[g]	B1[h]	583
Arable soil dust SDPA01 (Paulinenaue, Germany)	787	334	aspherical	Roger Funk[g]	B1[h]	385
Arable soil dust SDAr08 (Argentina)	910	407	aspherical	Roger Funk[g]	B1[h]	592
Arable soil dust SDWY01 (Wyoming, USA)	864	430	aspherical	Tom Hill[i]	B1[h]	623
Agricultural soil dust (Northern Germany)	561	249	aspherical	Roger Funk[g]	B1[h]	583
Urban dust	1329	1266	aspherical	NIST(1649a)	S	375
Illite_NX	825	260	sheet	Arginotec	S	807
Sea salt with skeletonema marinoi [j]	1212	338	cubic	Matt Salter[j]	B1	526

Note: For aerosol generation methods:

"A" represents for the method by using a nebulizer and a DMA (refer to the setup in Fig. 1) for sizing d_m=800 nm;

"B1" and "B2" represent the methods in which particles were sampled from AIDA and a stainless steel cylinder, respectively;

"S" corresponds to particles mobilized by shaking in a reservoir.

For particles size information, d_{va} values represent the expected values from Gaussian fitting to the particle sizes measured by LAAPTOF.

Spectra number is the number of averaged spectra.

[a]: These values represent the standard deviation from Gaussian fitting to the measured particle sizes (d_{va}).

[b]: There is only one weak but reproducible peak m/z 30 NO^+ in the positive spectra. Therefore we don't give the reference spectra in this paper.

[c]: SOA particles were formed in the Aerosol Preparation and Characterization (APC) chamber and then transferred into the AIDA chamber.

[d]: The nominal geometric size given by the manufacture Nanopartz Inc.

[e]: Electrical mobility equivalent diameter, d_m, measured by a scanning mobility particle sizer (SMPS).

[f]: The sizes (d_{va}) of Diesel particles and Saharan desert dust 2 are average values with their standard deviation.

[g]: Institute of Soil Landscape Research, Leibniz Centre for Agricultural Landscape Research, Germany.

[h]: Soil dust samples were dispersed by a rotating brush generator and injected via cyclones into the AIDA chamber.

[i]: Department of Atmospheric Science, Colorado State University, Fort Collins, Colorado, USA.

[j]: Samples, provided by Elena Gorokhova and Matt Salter at Stockholm University, they were prepared by diluting a pure skeletonema marinoi culture with artificial seawater (sigma sea salt) to conditions representative of a bloom in the ocean.

685 **Table 2: Summary of mass spectral patterns**

Species	Signature peaks in positive spectra	Signature peaks in negative spectra	Typical Peak Ratios histogram x_0 (width)*
potassium	39 K^+, 41 K^+		I39:I41=~**13.5**(0.9)
calcium	40 Ca^+, 56 CaO^+		
aluminium	27 Al^+	43 AlO^-, 59 AlO_2^-	
silicon	28 Si^+, 44 SiO^+	60 SiO_2^-, 76 SiO_3^-, 77 $HSiO_3^-$	(I76+I77):I60=~**1.0** (0.33)
silicon & aluminium	27 Al^+, 28 Si^+, 44 SiO^+	43 AlO^-, 59 AlO_2^-, 60 SiO_2^-, 76 SiO_3^-, 77 $HSiO_3^-$, 119 $AlSiO_4^-$, 179 $AlSiO_4.SiO_2^-$	
ammonium	18 NH_4/H_2O^+, 30 NO^+		
nitrate	30 NO^+	46 NO_2^-, 62 NO_3^-	
sulphate		32 S^-, 48 SO^-, 64 SO_2^-, 80 SO_3^-, 81HSO_3^-, 96 SO_4^-, 97 HSO_4^-,	
chloride		35 Cl^-, 37 Cl^-	(I35+I36):I37=~**3.1**(0.5)
elemental carbon	$12_n C_n^+$	$12_nC_n^-$	
organics		24 C_2^-, 25 C_2H^-, 26 C_2H_2/CN^-	
organic acids		45 $COOH^-$, 59 CH_2COOH^-, 71 CCH_2COOH^-, 73 $C_2H_4COOH^-$, 85 $C_3H_4COOH^-$, 99 $C_4H_6COOH^-$, 117 $(CO)_3OOH^-$	
nitrogen-containing organics		26 CN^-, 42 CNO^-	
unsaturated organics		25 C_2H^-, 26 $C_2H_2^-$ unknown fragments 49- and 73-	
aromatic compounds	77 $C_6H_5^+$, 91$C_7H_7^+$, 103 $C_8H_7^+$/105 $C_8H_9^+$, 115 $C_9H_7^+$	25 C_2H^-, 26 $C_2H_2^-$ unknown fragments 49- and 73-	

686

687 Note:
688 *We have made histograms for the three typical peak ratios, respectively (ref. Fig. S5). Histogram x_0 is the expected value that indicates the
689 position of the peak resulting from Gaussian fit, and the width is the corresponding standard deviation. I is short for the intensity of the
690 corresponding peak in LAAPTOF spectra; typical peak ratios for potassium and chloride are based on pure and mixed salt that containing K
691 and Cl; typical peak ratios for silicon are based on pure SiO_2.

692

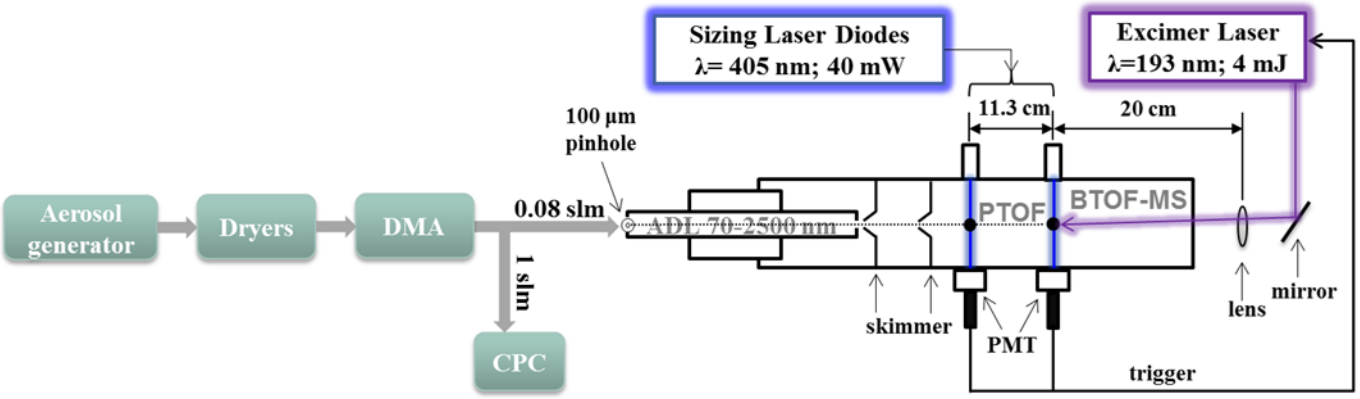

Figure 1: Schematic of the LAAPTOF instrument and the experimental setup for measuring standard samples (method A), e.g. PSL, NH_4NO_3 and K_2SO_4 particles, which were generated from a nebulizer, passed through two dryers, were size-selected by a differential mobility analyzer (DMA), and then measured by LAAPTOF.

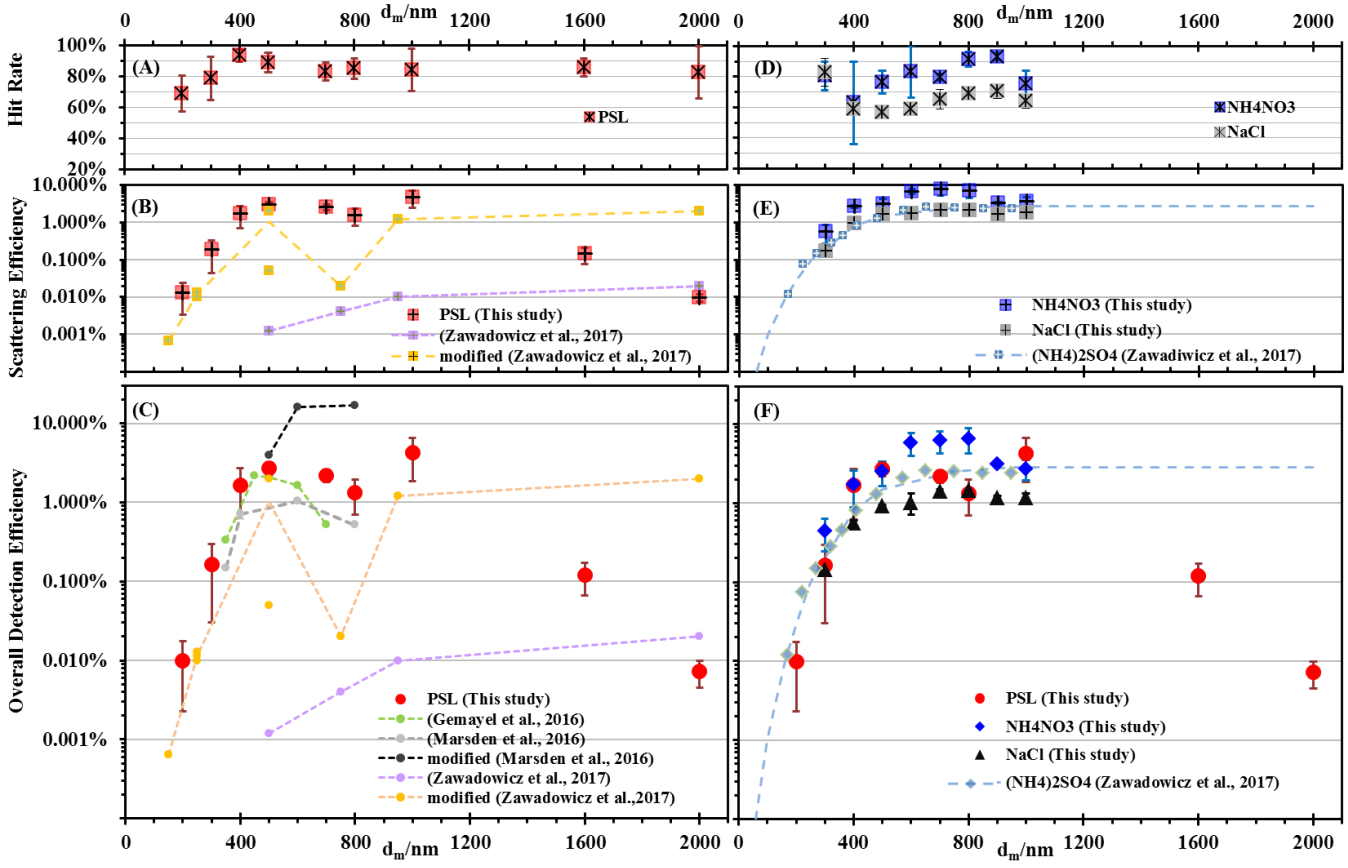

Figure 2: Hit rate (HR, panel A and D), scattering efficiency (SE, panel B and E), and overall detection efficiency (ODE, panel C and F) for PSL, ammonium nitrate (NH_4NO_3) and sodium chloride (NaCl) salt particles as a function of mobility diameter, d_m. Aerosol particles in this study were generated from a nebulizer and size-selected by DMA. In panel (B) and (E), optical counting efficiencies (OCE) for PSL and ammonium sulphate ($(NH_4)_2SO_4$) at the detection beam from the study by Zawadowlcz et al. (2017), corresponding to the SE defined in this study, are plotted for comparison. In panel (C) and (F), ODE for PSL and salt particles from other studies (Gemayel et al., 2016; Marsden et al., 2016; Zawadowicz et al., 2017) are plotted for comparison. In this figure, dashed lines are used only for guiding the eyes.

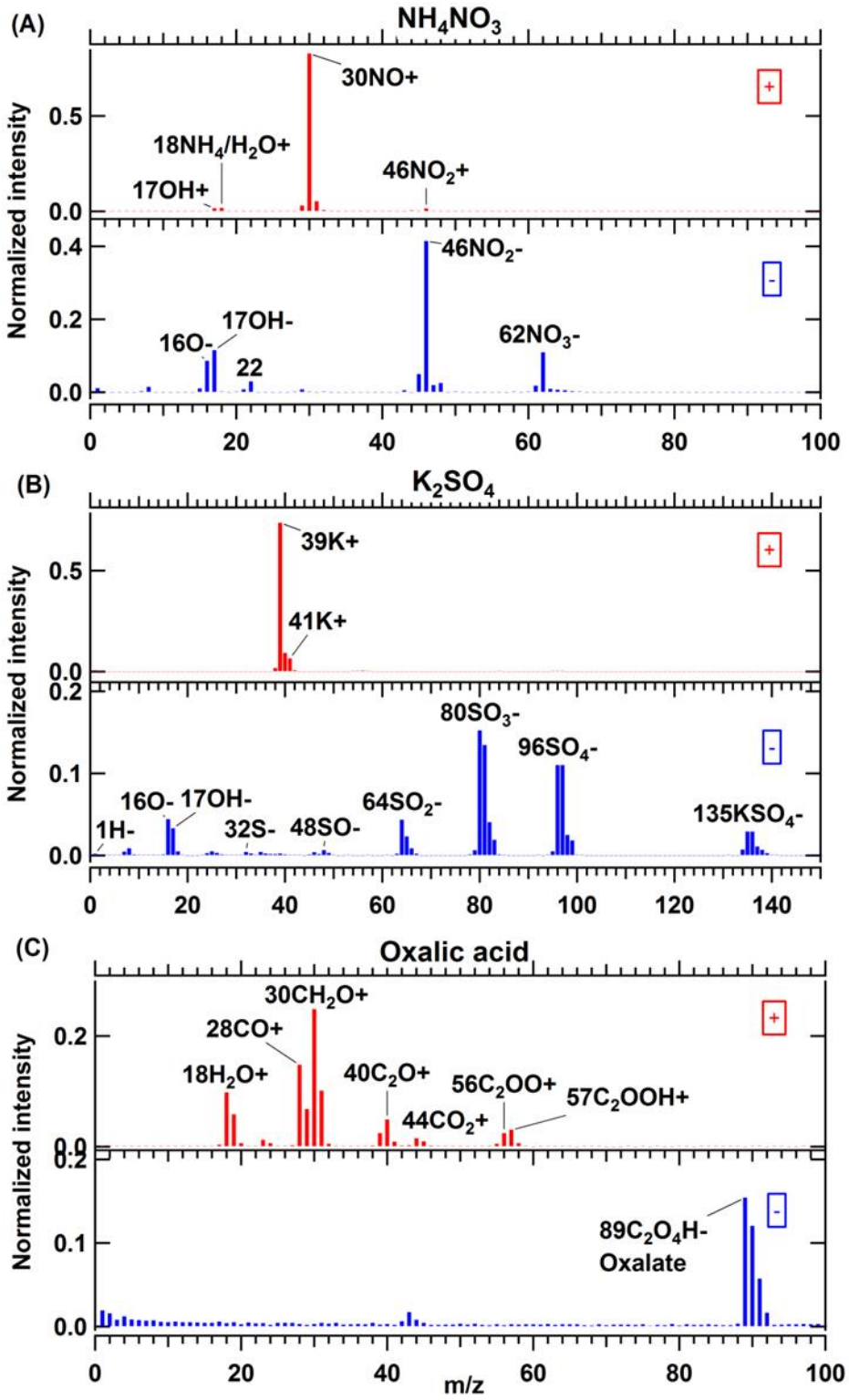

Figure 3: Average mass spectra for pure compound aerosol particles: (A) NH_4NO_3 (dva=1160 nm), 497 single spectra averaged, (B) K_2SO_4 (dva=1465 nm), 300 single spectra averaged, and (C) oxalic acid particles (dva=1081 nm), 736 single spectra averaged.

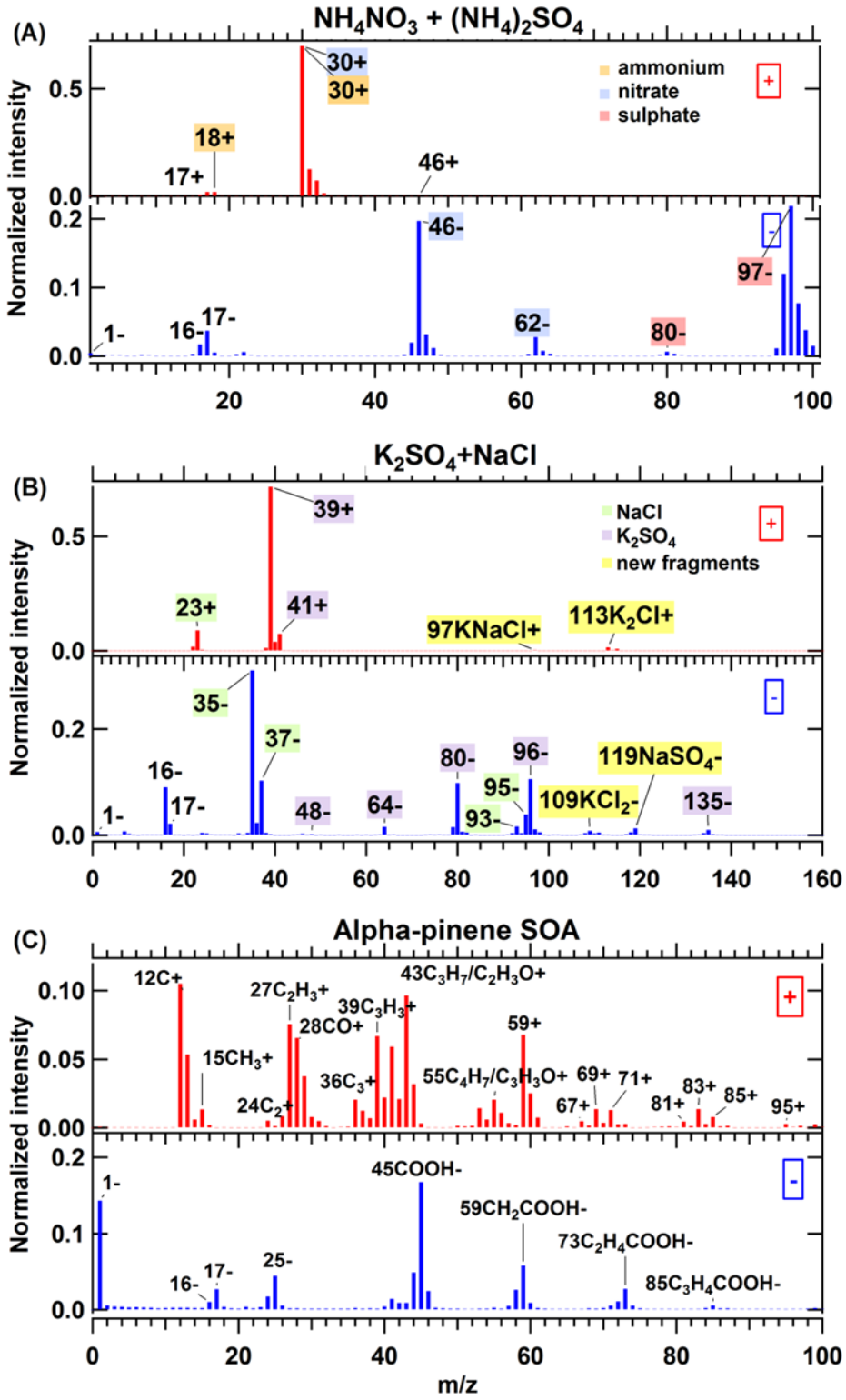

Figure 4: Average mass spectra for particles of internal mixtures of (A) NH_4NO_3 and $(NH_4)_2SO_4$, (d_{va}= 1102 nm), 454 single spectra averaged and (B) NaCl and K_2SO_4, (d_{va}= 1375 nm), 259 single spectra averaged as well and (C) secondary organic aerosol (SOA) particles from α-pinene ozonolysis, which was performed in the APC chamber, then the resulting particles were transferred into the AIDA chamber at 263 K and 95% RH, d_{va}= 505 nm, 1938 single spectra averaged. In panel (A), red, blue and orange label shadings represent fragments of sulphate, nitrate and ammonium, respectively. In panel (B), green and purple label shadings represent fragments from NaCl and K_2SO_4 components (see section 3.2.1) in the mixed particles, respectively; yellow label shadings represent the fragments only in the internal mixture of NaCl and K_2SO_4.

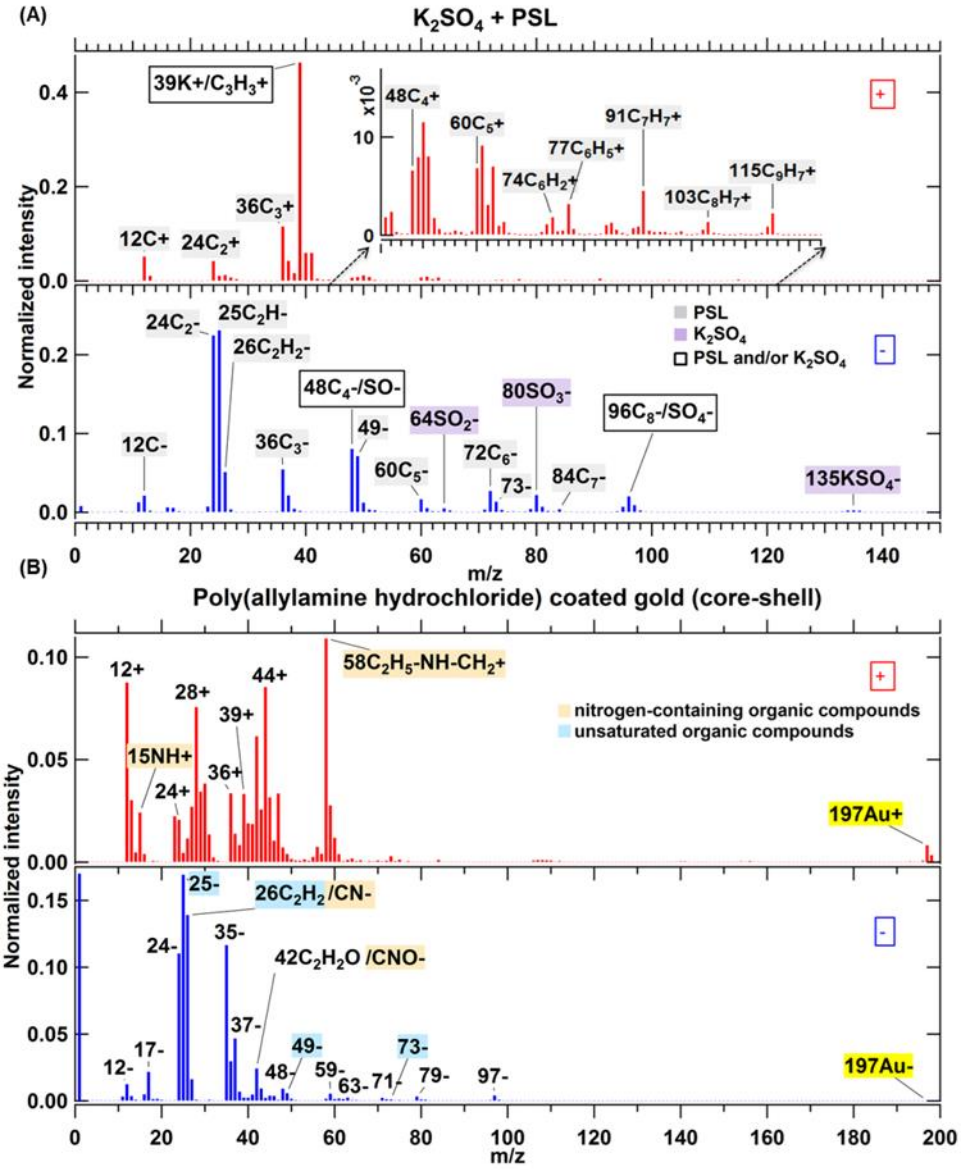

Figure 5: Average mass spectra for core-shell particles of (A) PSL coated with K_2SO_4, d_{va}= 805 nm, 609 single spectra averaged, and (B) poly(allylamine hydrochloride) coated gold (Au) particles with geometric 300 nm gold core and 50 nm thick organic shell, 417 single spectra averaged. In panel (A), grey and purple label shadings represent the fragments arising from pure PSL and pure K_2SO_4 components, respectively; box labels represent the fragments with contributions from core and shell compounds. In panel (B) orange and blue label shadings represent the fragments arising from nitrogen-containing and unsaturated organic compounds, respectively, and yellow label shadings represent gold.

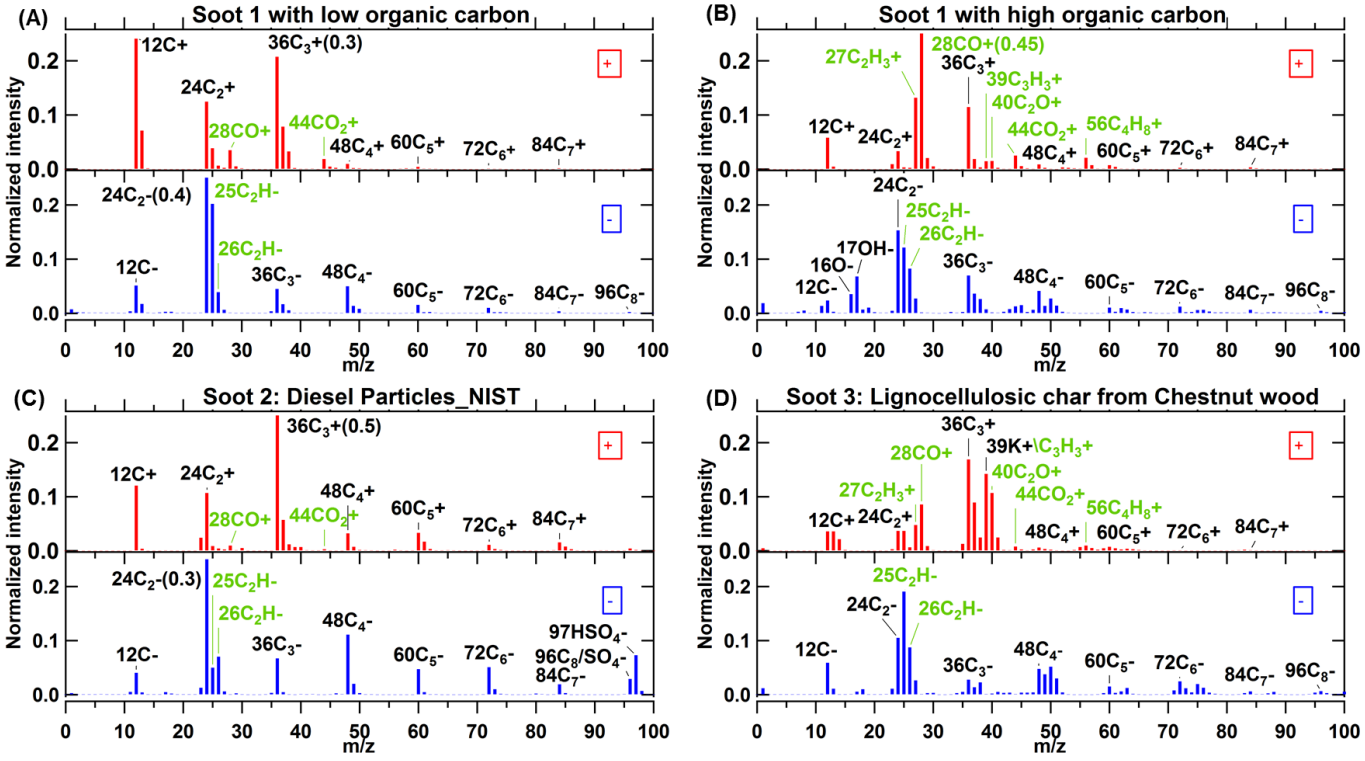

Figure 6: Average mass spectra for soot particles with (A) high elemental carbon (EC), low organic carbon (OC) content and (B) low EC and high OC from combustion of propane in a soot generator and transferred to a stainless steel cylinder of ~0.2 m^3 volume, as well as soot particles of (C) diesel particles (NIST) and (D) lignocellulosic char from chestnut wood. In panel (A) and (C), the numbers in brackets beside peak 36^+ and 24^- are the exact intensity values for them. The OC signatures are labelled in green. The numbers of spectra averaged for each spectrum are 617 (A), 347 (B), 533 (C) and 390 (D).

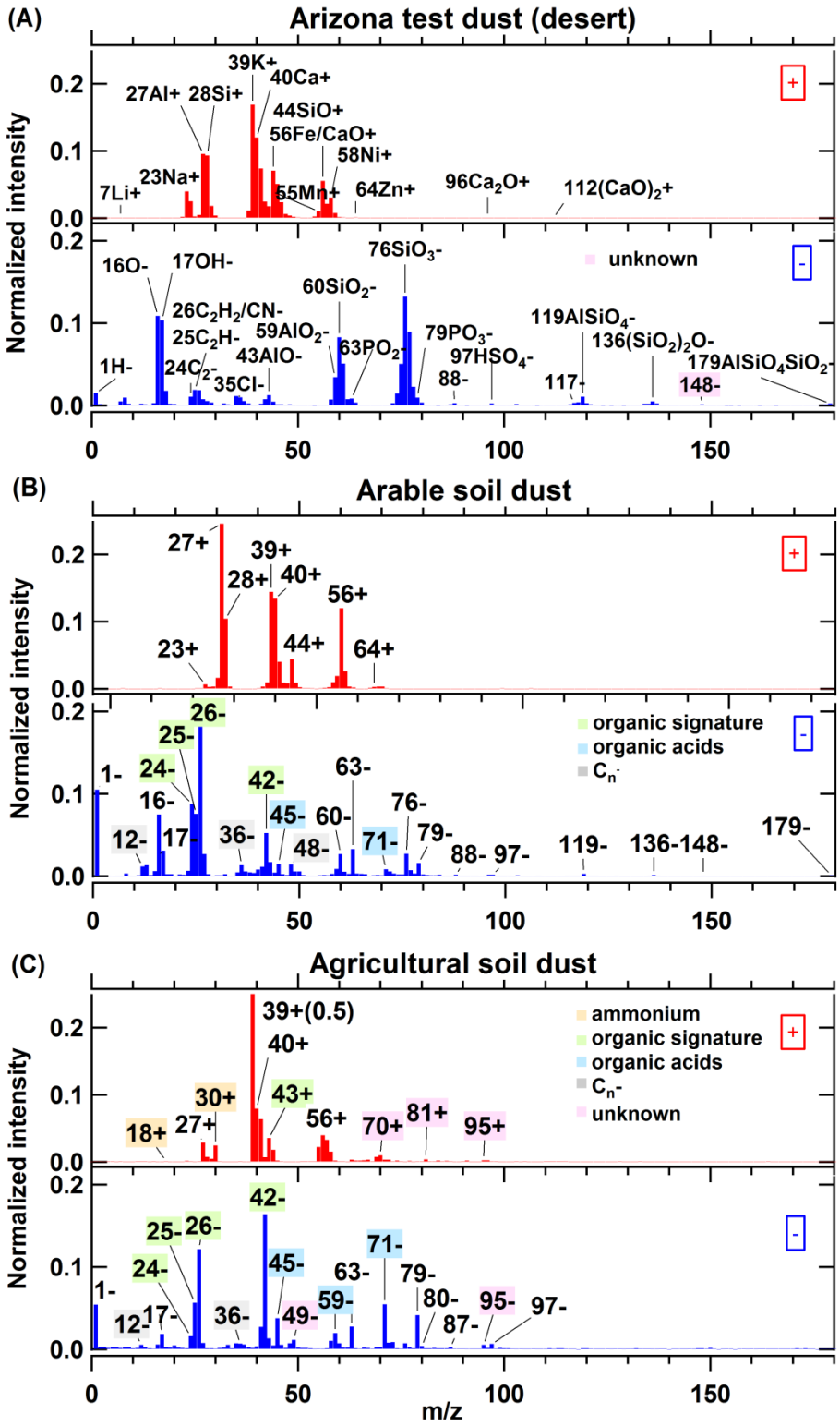

Figure 7: Average mass spectra for particles of complex mixtures: (A) Arizona test dust (desert dust), directly sampled into the LAAPTOF from a shaked bottle (B) arable soil dust, collected from Gottesgabe in Germany, was dispersed by a rotating brush generator and injected via cyclones into the AIDA chamber at 256 K and 80% RH, and (C) agricultural soil dust, collected from harvesting machines after rye and wheat harvest, were generated by using the same method as (B). For panel (B) and (C), fragments labelled in green represent more intensive organic signatures in soil dust particles; grey labels represent EC patterns; blue labels represent organic acids; orange labels represent ammonium salts; red labels represent unknown fragments. The numbers of spectra averaged for each spectrum are 261 (A), 583 (B), and 286 (C).

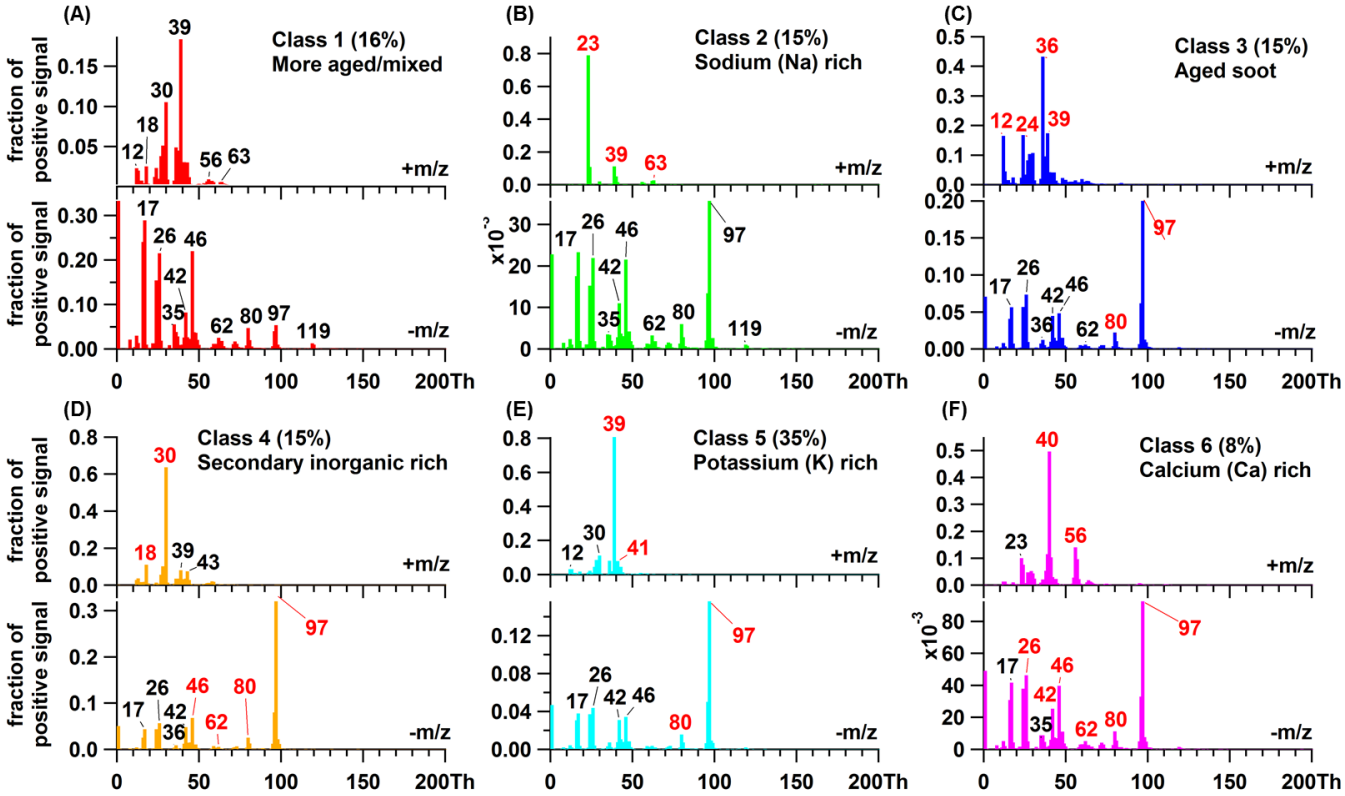

Figure 8: Mass spectra for six classes of particles measured on July 29th, 2016 during the field campaign TRAM01, based on classification according to Fuzzy c-means algorithm. The percentage in each pair of spectra (A to F) gives us information about the similarity of the total aerosols to different classes. The red tags represent the signatures for each typical class, but there is no red tag in spectra B, since this class is more aged particles that containing signatures for different classes. Mean particle size: d_{va} (676±165) nm.

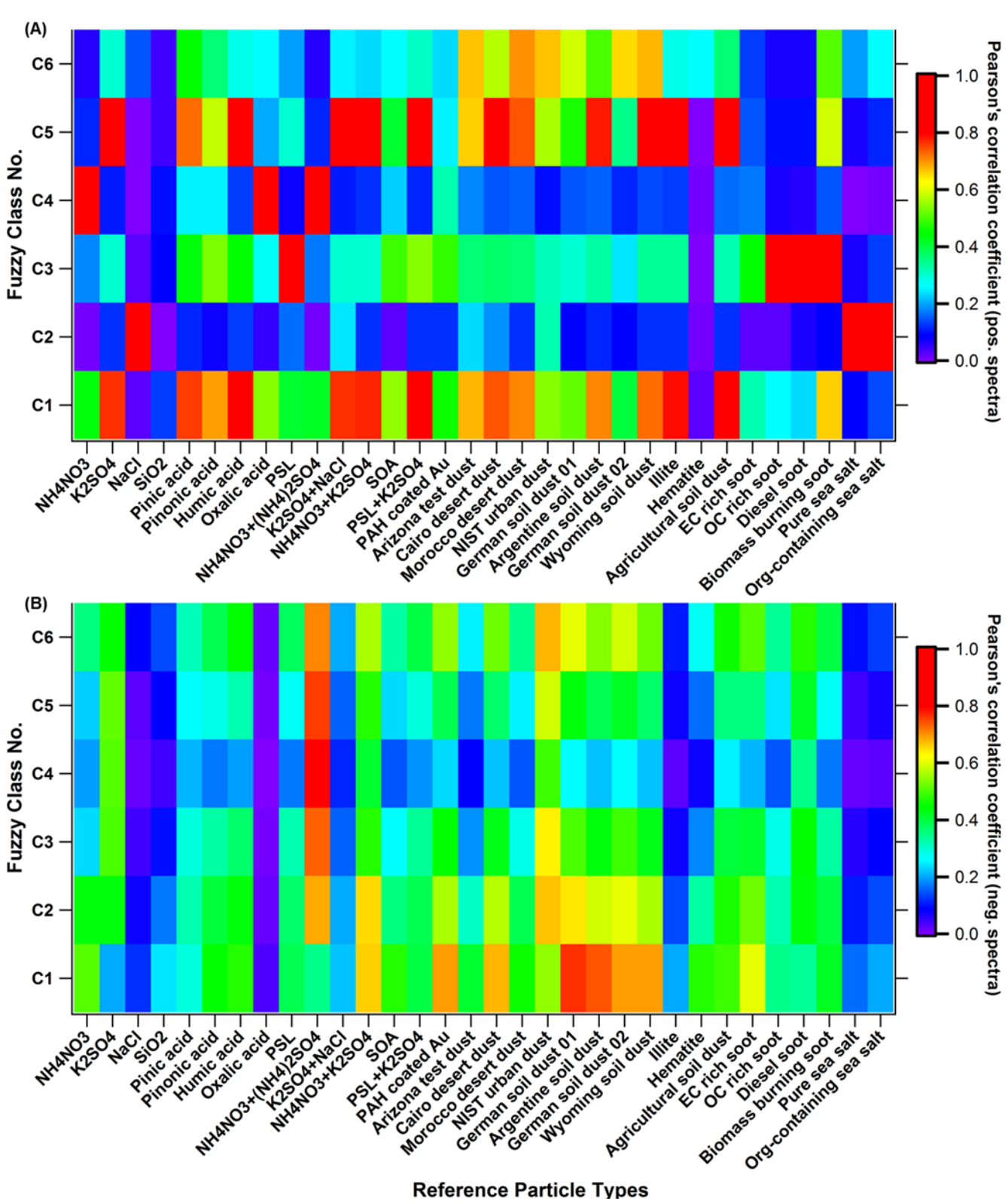

Figure 9: Correlation between Fuzzy classification results (6 classes, C1 to C6) and laboratory-based reference spectra. Panel (A) and (B) are the correlation results for the positive and negative spectra, respectively. PAH is short for poly(allylamine hydrochloride), biomass burning soot is the lignocellulosic char from chestnut wood.

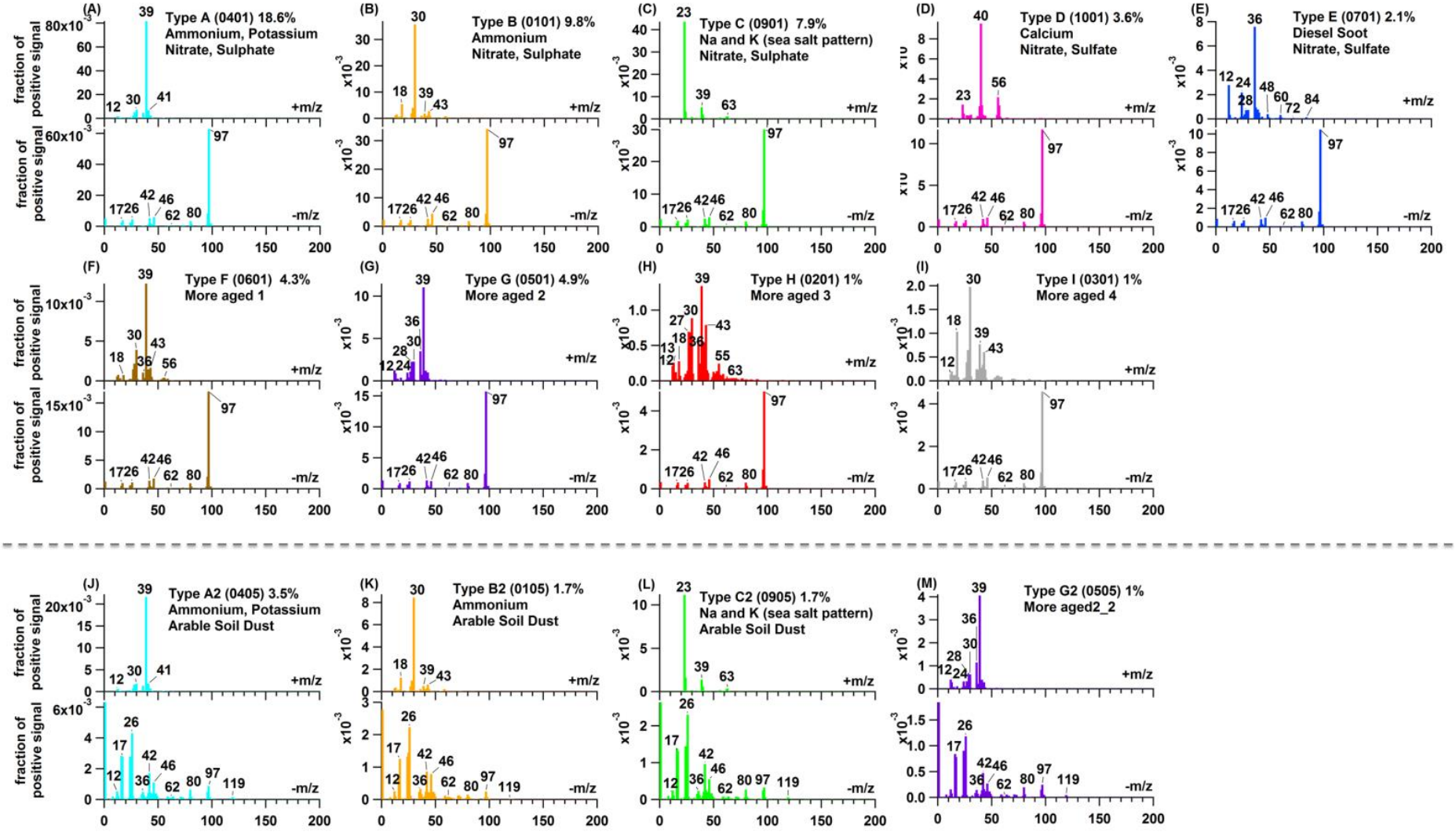

Figure 10: Mass spectra for 13 different types of particles measured on July 29th, 2016 during the field campaign TRAM01, based on the classification according to laboratory-based reference spectra. The 4 digits codes in the brackets represent particle types (refer to Table S2). The % values are the particle number fractions. For panel A to E and J to L, there are two lines for the names, the first and second lines correspond to the highly correlated positive and negative references, respectively.